https://doi.org/10.1021/acs.nanolett.0c01484 https://pubs.acs.org/doi/10.1021/acs.nanolett.0c01484

Highly Efficient Polymeric Carbon Nitride Photoanode with Excellent Electron Diffusion Length and Hole Extraction Properties

Neeta Karjule,[a] *Jesús Barrio,*[a] *Lidan Xing,*[b] *Michael Volokh*[a] *and Menny Shalom*[a]*

[a]*Department of Chemistry and Ilse Katz Institute for Nanoscale Science and Technology, Ben-Gurion University of the Negev, Beer-Sheva 8410501, Israel*

[b]*School of Chemistry, South China Normal University, Guangzhou 510006, China*

ABSTRACT

Polymeric carbon nitride (CN) has emerged as a promising semiconductor in photoanodes for photoelectrochemical cells (PEC) owing to its suitable electronic structure, tunable band gap, high stability, and low price. However, the poor electron diffusion within the CN layer and hole extraction to the solution still limit its applicability in PECs. Here, we report the fabrication of a CN photoanode with excellent electron diffusion length and remarkable hole extraction properties by careful design of its electronic interfaces. We combine complementary synthetic approaches to grow tightly packed CN layers forming a type-II heterojunction, which results in a CN photoanode with excellent charge-separation, high electronic conductivity, and remarkable hole extraction efficiency. The optimized CN photoanode displays excellent PEC performance,

reaching up to 270 μA cm^{-2} in a 0.1 M KOH solution at 1.23 V vs. RHE, extremely low onset potential (~0.0012 V), and long-term stability up to 18 h.

Keywords: Carbon nitride, photoelectrochemical cells, water splitting, photoanode

Water-splitting photoelectrochemical cell (PEC) technology can potentially convert sunlight and water to clean and cheap hydrogen fuel.[1] Practical PEC-mediated hydrogen production requires robust and efficient semiconductors (SC), with good light-harvesting properties, high charge-separation efficiency, suitable energy band positions, and stability in harsh conditions alongside low price.[2] Recently, polymeric carbon nitrides (CN) have emerged as new and promising SCs for PEC,[3] owing to their tunable band gap, suitable energy bands, high stability, and low cost.[4,5] However, despite their advantages and proven performance, to date, progress on CNs' utilization as PEC photoanodes has been limited by the poor charge-separation and fast recombination under illumination. In the last years, we and others proposed several methods to increase charge-separation and electron (e^-) mobility within the CN layer and hole (h^+) extraction to the solution.[6-8] The enhancement of charge-separation under illumination can be obtained by the formation of a new electronic configuration, for example from heterojunctions or defects,[9–12] or by facilitating the transfer of e^-–h^+ pairs to another medium (to another SC layer, a catalyst, or the solution).[13-15] A significant improvement in the e^- diffusion toward the conductive substrate can be achieved by the introduction of an e^- acceptor layer (e.g. TiO_2, reduced graphene oxide),[16,17] and/or by doping the CN with C-C bonds.[18,19] The latter alters the electronic conductivity within the CN, thanks to the increase in the number of delocalized electrons within its framework. Longer e^- diffusion length allows in turns a better light harvesting thanks to the use of a thicker absorber layer. For water-splitting, h^+ extraction and the production of oxygen

are considered more challenging, owing to the sluggish kinetics and the 4 e^-–h^+ pairs involved in the process. In the presence of hole scavengers as triethanolamine or redox electrolytes (e.g. polysulfide),[20,21] h^+ extraction efficiencies can be dramatically increased, owing to the fast e^-–h^+ transfer. Recently, it was demonstrated that charge transfer and h^+ extraction properties in CN-PEC are correlated to the order within the CN.[22,23] In the case of a better stacking order of the graphitic layers, a hole extraction efficiency of ~47% was obtained.[24] However, in all the above-mentioned scenarios, only one problem was tackled either e^- diffusion or h^+ extraction due to synthetic limitations. Therefore, a new CN electrode design, which enables achieving both better e^- diffusion and enhanced h^+ extraction efficiency is needed for a substantial improvement in performance.

We report the design of a CN photoanode with excellent e^- diffusion length and remarkable h^+ extraction properties. To do so, we developed a new synthetic method that results in the growth of ordered CN layers on top of reduced graphene oxide (rGO). Moreover, to further improve the charge-separation, we built a type-II heterojunction by growing a second CN layer by thermal vapor condensation (TVC).[19] Detailed structural and photoelectrochemical analysis revealed the presence of highly ordered CN layers, which are directly connected to rGO, gives up to 50% h^+ extraction efficiencies over a wide potential range, along with good e^- conductivity. The resulting modified CN film displays remarkable PEC performance that is beyond the state-of-the-art for CN materials, reaching up to 270 μA cm^{-2} in a 0.1 M KOH solution at 1.23 V vs. RHE, and extremely low onset potential, as well as long-term stability, up to 18 h.

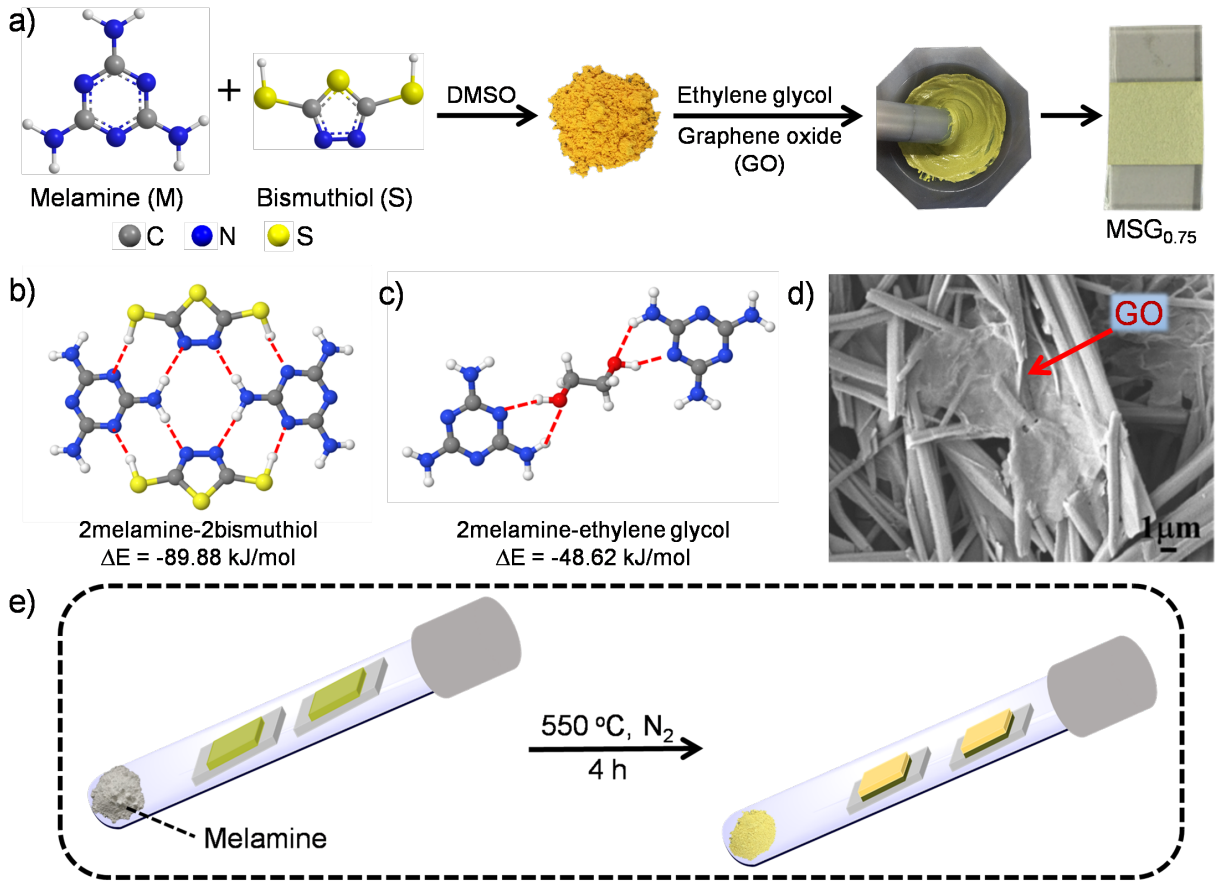

Figure 1. a) Electrode preparation scheme: a supramolecular complex comprising melamine and bismuthiol is formed, ground, and blended into a paste with ethylene glycol and GO, which is doctor-bladed onto an FTO substrate to get melamine-bismuthiol-graphene oxide$_{0.75}$ ($MSG_{0.75}$) films. b) DFT simulation of the interaction energy between melamine-bismuthiol supramolecular assemblies. c) DFT simulation of the interaction between ethylene glycol (EG) with melamine-bismuthiol supramolecular assembly. d) SEM image of $MSG_{0.75}$ films on FTO before calcination. e) Schematic representation of CN electrodes formation *via* thermal polymerization and condensation in the presence of melamine powder in the tube (enabling the TVC), which is covered with an aluminum foil.

Supramolecular films were prepared from supramolecular assemblies deposited using the doctor-blade technique.[25,26] An illustration of the growth of homogeneous supramolecular films on fluorine-doped tin oxide (FTO) electrodes from a sulfur-containing monomer, bismuthiol (S), and melamine (M) is shown in Figures 1a and S1a (MS).[27] Scanning electron microscopy (SEM) of the hydrogen-bonded framework (MS(DMSO)) indicates ordered aggregate of stick-like structures with an approximate length of several μm (Figure S1b). Fourier-transform infrared spectroscopy (FTIR) and powder X-ray diffraction (XRD) confirm the formation of a supramolecular complex between the monomers (see discussion at Figure S2). Density functional theory (DFT) simulations revealed the most probable supramolecular structure (Figure 1b and S3c–e), owing to its higher E_{int} (-89.88 compared to -70.68 kJ mol^{-1}). The calculated E_{int} between melamine and ethylene glycol (EG, -48.62 kJ mol^{-1}) is lower than between bismuthiol and EG (-44.41 kJ mol^{-1}), indicating that the EG would preferentially bind to melamine (Figure 1c and Figures S4–S5). To prepare homogeneous supramolecular films (MS), these assemblies were blended with EG, forming a very smooth paste, which was subsequently doctor-bladed over the electrodes (Figure S6). The thickness of the films was manipulated by varying the number of scotch-tape layers (L).

Additionally, different amounts of graphene oxide (GO) were mixed with the prepared supramolecular assembly and deposited on FTO in the same manner in order to obtain MSG$_x$ electrodes (where x corresponds to the volume of GO suspension added to the sample, x = 0.25, 0.5, 0.75, and 1.0 mL) (Figures 1a and S7). Cross-section SEM images of FTO with MS (L = 3) shows the formation of a thick (*ca*. 67 μm) layer of the supramolecular assembly (Figure S8b). A similar procedure with incorporated GO, *i.e*., an MSG$_{0.75}$ layer, resulted in a thinner layer (*ca*. 43 μm, Figure S8d). Top-view SEM shows that GO sheets form bridges between the MS

supramolecular aggregates (Figure 1d). On the other hand, the rod-like morphology of MS powder was fully preserved upon deposition over FTO, as shown in Figure S8. Reference melamine films were prepared in the same manner with only melamine ground in EG. A cross-section SEM image of the melamine film shows the formation of a very thick (~180 μm) layer of melamine on the FTO (Figure S9). FTIR and XRD of the melamine and MS films display similar features to the powder counterpart (Figure S10). The chemical states of MS and $MSG_{0.75}$ films were investigated by X-ray photoelectron spectroscopy (XPS, Figures S11–S12).

Carbon nitride films were obtained by calcination of the prepared supramolecular films at 550 °C under N_2 (Figure 1e). To improve the deposition and the CN attachment to the FTO, melamine vapor was formed during the thermal condensation: melamine powder at the bottom of the reaction vessel tube (Figure 1e) sublimes upon heating and is deposited as a second CN layer from the gas-phase onto the layer derived from the supramolecular assemblies as shown in Figure 2 (the second CN layer, which corresponds to the sublimed melamine (*via* the TVC process) is marked with red double-headed arrows). This method allows the formation of a very compact and consistent CN layer over FTO electrodes. The CN films that were prepared without melamine powder inside the tube were less uniform and showed lower PEC performance, as shown later (Figure S13). Surface and cross-section morphologies of CN-MS/M and CN-$MSG_{0.75}$/M electrodes, which were doctor-bladed (L = 3), are shown in Figure 2b–c. The SEM images show a good coverage of both layers over the FTO substrate, with a similar morphology consisting of aligned microstructures. For CN-MS/M, the thickness of the first layer (Semiconductor I) is estimated at ~65 μm, whereas the thickness of the second layer (Semiconductor II) is 39 μm. For CN-$MSG_{0.75}$/M, the thicknesses are 45 and 42 μm, respectively. Energy-dispersive X-ray spectroscopy (EDS) mapping further demonstrates the existence of C,

N, and S in the CN films (Figure S14). In the case of the reference CN-M electrodes, the obtained film shows less uniform coverage around the FTO (Figure S15). Elemental analysis (Table S1) confirms the presence of C, N, H, and S in the supramolecular films as well as in the derived CN electrodes. The C/N ratio is higher in CN-MSG$_{0.75}$/M than in CN-MS/M, reflecting the incorporation of rGO in the CN film (as the GO in the supramolecular paste is thermally reduced to rGO during the thermal condensation).[28] Hereafter the CN-MSG$_{0.75}$/M electrode is denoted as CN-MSG/M for clarity.

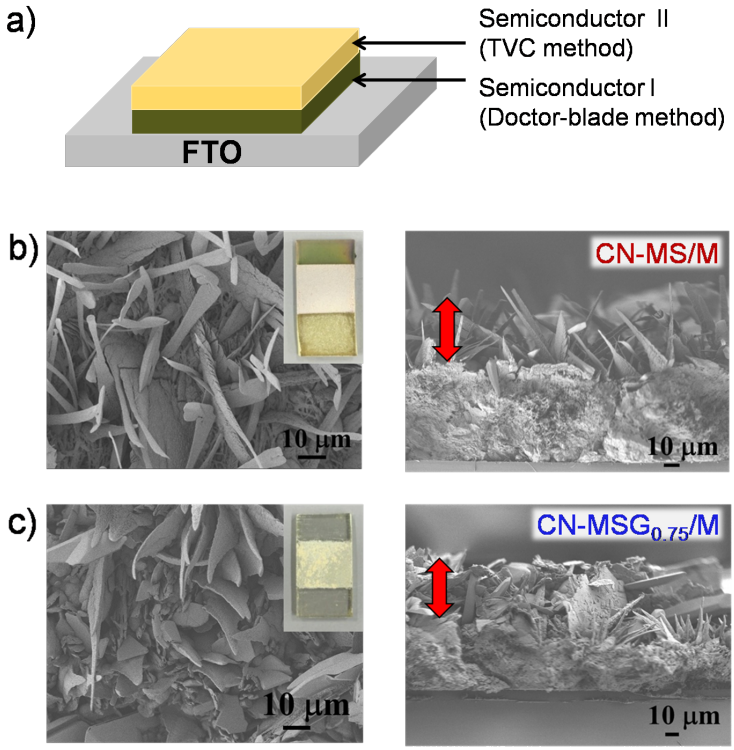

Figure 2. a) Schematic presentation of forming type-II heterojunction by growing two different SC CN layers. SEM images of CN electrodes, which were prepared in the presence of melamine powder in the reaction vessel: b) Top-view and cross-section of CN-MS/M. c) Top-view and cross-section of CN-MSG$_{0.75}$/M.

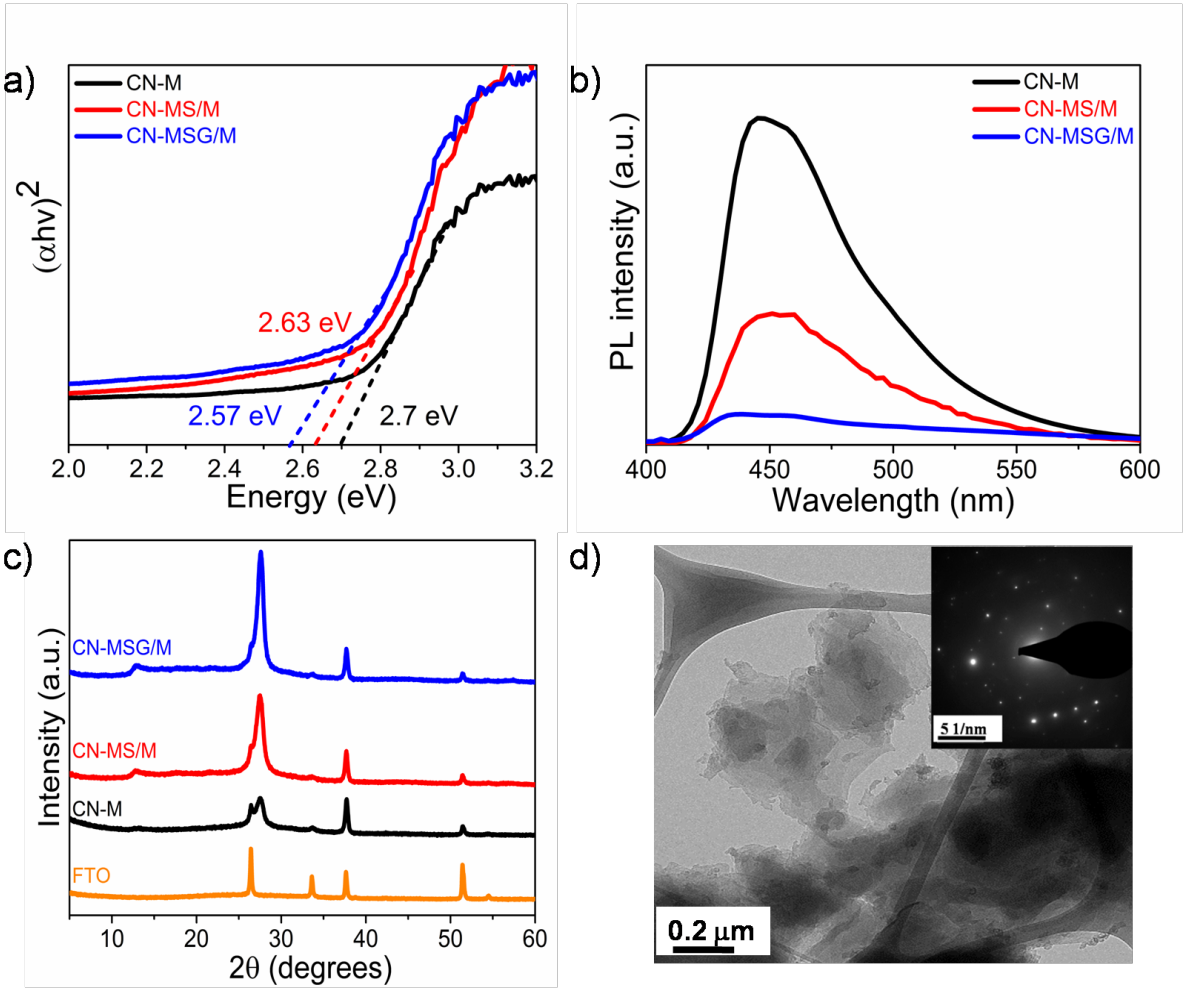

Figure 3. a) Optical (direct) band gap estimation of the CN films using the Tauc plot method. b) PL spectra of CN electrodes. c) XRD patterns of the CN electrodes. d) TEM images of CN-MSG/M with the corresponding selected-area electron diffraction (SAED) pattern.

The absorption spectra of the CN films (Figure S16) showed a slight red-shift of the absorption edge for the CN-MSG/M electrode, from 2.63 eV for CN-MS/M to 2.57 eV for CN-MSG/M (Figure 3a). It is attributable to the presence of rGO, which gives a wide optical scattering all over the visible region. The photoluminescence (PL) spectra show a prominent quenching of the fluorescence intensity of CN-MS/M and CN-MSG/M in comparison to CN-M; this may stem from alternative non-radiative recombination paths within the films, which are

induced by surface states or by the heterojunction formation (Figure 3b).[29] Mott–Schottky measurements were utilized to evaluate the flat-band potential of the CN electrodes; the materials showed a positive slope indicative of an n-type behavior. Additionally, the conduction band edge of the modified CN electrodes is shifted towards a more positive potential than the one of CN-M (Figure S17). To further understand the interfacial charge-separation and transfer processes, the CB and VB edge positions were acquired from Mott-Schottky plots and UV-vis absorption (Figure S18). CN-MS (Semiconductor I) and CN-M (Semiconductor II) form a type-II heterojunction (Figure S18b). These results indicate that upon illumination, excited e^- migrate from the CB of Semiconductor II to that of Semiconductor I followed by collection at the FTO, while photogenerated h^+ travel in the opposite direction. Such interface allows charge-separation of photogenerated e^- and h^+, which reduces recombination.[30,31] We note that due to the similarity of the two layers it is very difficult to fully characterized their interface. FTIR spectra (Figure S19) and XRD patterns (Figure 3c) indicate the formation of a layered CN. CN-MS/M and CN-MSG/M show higher intensity at 27.5°, corresponding to the (002) crystal plane, which stands for a higher order in the corresponding films, while the (100) plane can be observed *ca*. 13°.

As previously reported, the addition of a sulfur-containing monomer can modify the texture of the CN network during the polymerization process, which results in a better crystal packing.[32–34] The structure of the CN nanosheets was analyzed by transmission electron microscopy (TEM). CN-MS/M and CN-MSG/M display thinner and more crystalline nanosheets in comparison with CN-M (Figures 3d and S20). Furthermore, the selected-area electron diffraction (SAED) pattern of CN-MS/M and CN-MSG/M, with (002) and (100) diffraction rings, illustrate the crystalline structure of the prepared CN films, while a much less intense diffraction ring was observed for CN-M. The rings corresponding to *d*-spacings of 3.24 and 6.80

Å are attributed to the (002) and (100) reflections of CN, supporting the XRD pattern. EDS analysis of CN-MSG/M confirmed the existence of C, N, and S in the film (Figure S21). The XPS spectra for C1s, N1s, and S2p of the CN electrodes confirm the formation of CN polymers and suggest the presence of residual sulfur doping (Figures S22–S24).

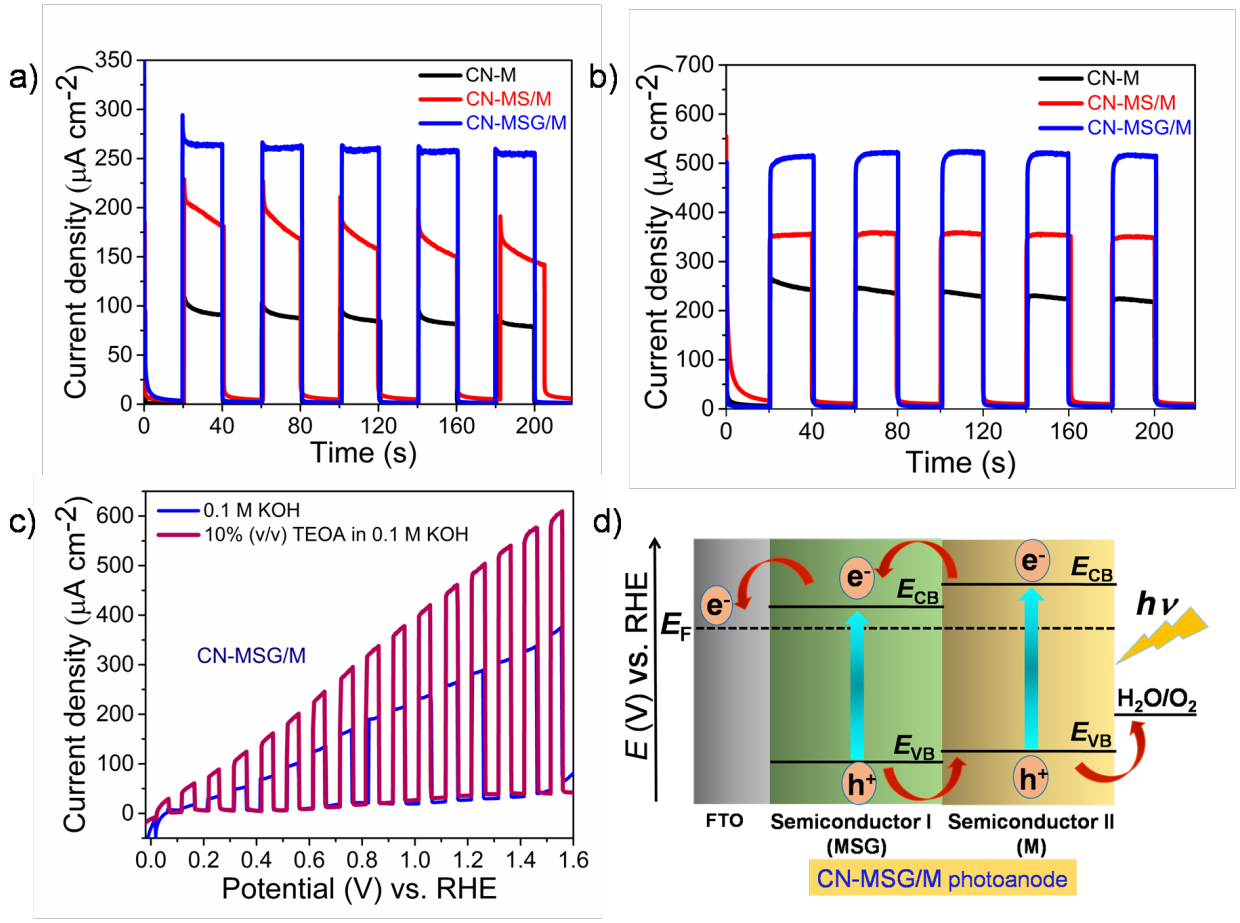

Figure 4. a) Photocurrent density of CN electrodes at 1.23 V vs. RHE in 0.1 M KOH. b) Photocurrent density CN electrodes at 1.23 V vs. RHE in 0.1 M KOH aqueous solution containing 10% (v/v) triethanolamine (TEOA). c) LSV curves of CN-MSG/M electrodes in 0.1 M KOH (blue) and 0.1 M KOH aqueous solution containing 10% (v/v) TEOA (purple) as a hole scavenger upon on/off light illumination. d) Possible charge transfer mechanism illustrated on a

suggested energy band diagram of the reported CN heterojunctions (type-II heterojunction between two CN-based SCs).

As discussed earlier, the CN-M films were prepared using the doctor-blade process with a number of scotch tape layer, L = 1, 2, 3, and 4. The effect of the thickness over the PEC performance was studied and the highest photocurrent density (84 μA cm^{-2} at 1.23 V vs. RHE) was obtained for 3 scotch tape layers (Figure S25). Consequently, we decided to utilize thereafter L = 3 for preparation of the first CN layer. Upon addition of melamine powder into the tube during calcination, the photocurrent density of CN-M/M turns poor and unstable due to the increase in thickness of the final film on the photoanode, which results in higher recombination rate and charge transfer resistance (Figure S26). Nevertheless, the photocurrent density of sulfur-modified CN-MS/M reached up to 160 μA cm^{-2} (at 1.23 V vs. RHE), a two-fold increase compared to CN-M (Figure 4a). This difference can be attributed to an improved charge-separation and electric conductivity of CN-MS/M in comparison to CN-M. In order to investigate the charge transfer and migration, the photocurrent densities were analyzed under front- and back-side illumination (Figure S27). Back-side illumination results in a higher photocurrent density, disclosing that upon front irradiation, some of the e^-–h^+ pairs recombine before reaching the FTO due to the film's thickness. The initial spike current in CN-M and CN-MS/M photoanodes (Figure 4a) may be attributed to fast photoexcited charge recombination.[35]

The addition of GO to MS during the blending process, before the film preparation, dramatically alters the PEC performance after calcination; the photocurrent density measurements of CN-MS/M electrodes after the addition of different amounts of GO (CN-MSG_x/M) consistently show a strong performance enhancement (Figures 4a and S28). The CN-

$MSG_{0.75}$/M electrode (denoted as CN-MSG/M) exhibits the highest photocurrent, reaching up to 270 μA cm^{-2} at 1.23 V vs. RHE (Figure 4a), which is among the highest reported for a CN-photoanode (Table S2). A further increase of GO content (*i.e.*, CN-MSG_1/M) slightly decreases the photocurrent density despite maintaining the stability upon repeated cycles, which is probably due to a diminished light harvesting by the electrode. In the case of CN-$MSG_{0.75}$/M (or CN-MSG/M), rGO is promoting the charge-separation and increases the electric conductivity, which ultimately results in higher photocurrents. The significantly lower photocurrent spike in CN-MSG/M is attributed to lower recombination rate, illustrating higher e^- conductivity and e^- diffusion in the films caused by rGO. To scrutinize the diffusion length of photoexcited charges within CN-MS/M and CN-MSG/M electrodes, we measured the photocurrent density as a function of thickness (Figure S29) and upon back- and front-side illumination (Figure S30). The photocurrent densities linearly increased up to an electrode thickness of ~40 μm. CN films (CN-MS and CN-MSG) that were prepared without melamine powder inside the tube showed lower performance (Figure S31).

The modified CN electrodes display a significant photoelectrochemical activity in terms of onset potential and photocurrent density (Figure S32). The onset potential of both CN-MS/M (0.06 V vs. RHE) and CN-MSG/M (0.0012 V vs. RHE) are shifted to low values compared to a CN-M electrode (0.17 V vs. RHE). This shift indicates an enhanced charge-separation, which is credited to the enhanced conductivity resulting from the addition of rGO, and a better packing of the CN layer, which facilitates hole extraction. The photocurrent density of the CN electrodes was also characterized in the presence of triethanolamine (TEOA) as a hole scavenger (10% (v/v) TEOA in 0.1 M KOH). Under these conditions, maximal h^+ extraction is assumed. The CN-MS/M and CN-MSG/M electrodes exhibit a two-fold photocurrent density enhancement

compared to the experiment without TEOA, owing to improved h^+ extraction, reaching 350 μA cm^{-2} and 510 μA cm^{-2} at 1.23 V vs. RHE, respectively (Figure 4b). Figure 4c shows the *j–V* curves of CN-MSG/M under a periodic illumination with and without hole scavenger. The photocurrent density of the CN electrode increases linearly with increasing potentials in both 0.1 M KOH and 10% (v/v) TEOA in 0.1 M KOH. Furthermore, the charge transfer efficiency (η_t, %) (or hole extraction efficiency) from 0.2 V to 1.23 V vs. RHE results in values up to 46% and 53% for CN-MS/M and CN-MSG/M, respectively, while that of the CN-M electrode is 28% (Figure S33). Interestingly, the CN-MSG/M electrode exhibits steady charge transfer efficiency over the whole potential range, demonstrating the lower activation energy for charge-separation and water oxidation. This difference can be attributed to (i) the better layer packing, as well as (ii) the improvement in the conductivity and e^- diffusion by the presence of rGO. Furthermore, (iii) the formation of a type-II heterojunction as a result of the two different layers conforming the CN electrodes (MS/MSG and M) further facilitates the charge-separation within the layer (Figure S34).[36] Together, these three factors promote the separation of charge carriers, their transfer, and a more efficient water oxidation at the surface (Figure 4d). Electrochemically active surface area (ECSA) measurements reveal an increase in the electrochemically active species in the CN-MS/M electrode compared to the CN-M electrode. The addition of rGO leads to another enhancement, owing to the improved e^- conductivity (Figure S35). N_2 sorption analysis confirms a specific surface area enhancement: namely, 8.18 and 12.82 $m^2\ g^{-1}$ for CN-MS/M and CN-MSG/M, respectively (Figure S36).

Incident photon-to-current efficiency (IPCE) measurements at 1.23 V vs. RHE (Figure 5a) unveil values up to 17.1% at 380 nm and 9.8% at 420 nm for CN-MSG/M, with a photoresponse onset at 480 nm, which is consistent with the UV-vis absorption. Electrochemical

impedance spectroscopy (EIS) measurements revealed a decrease in charge transfer resistance (R_{ct}) (Figures 5b and S37). This result implies a better h^+ extraction from the CN-MS/M and CN-MSG/M electrodes than from the CN-M electrode.[37]

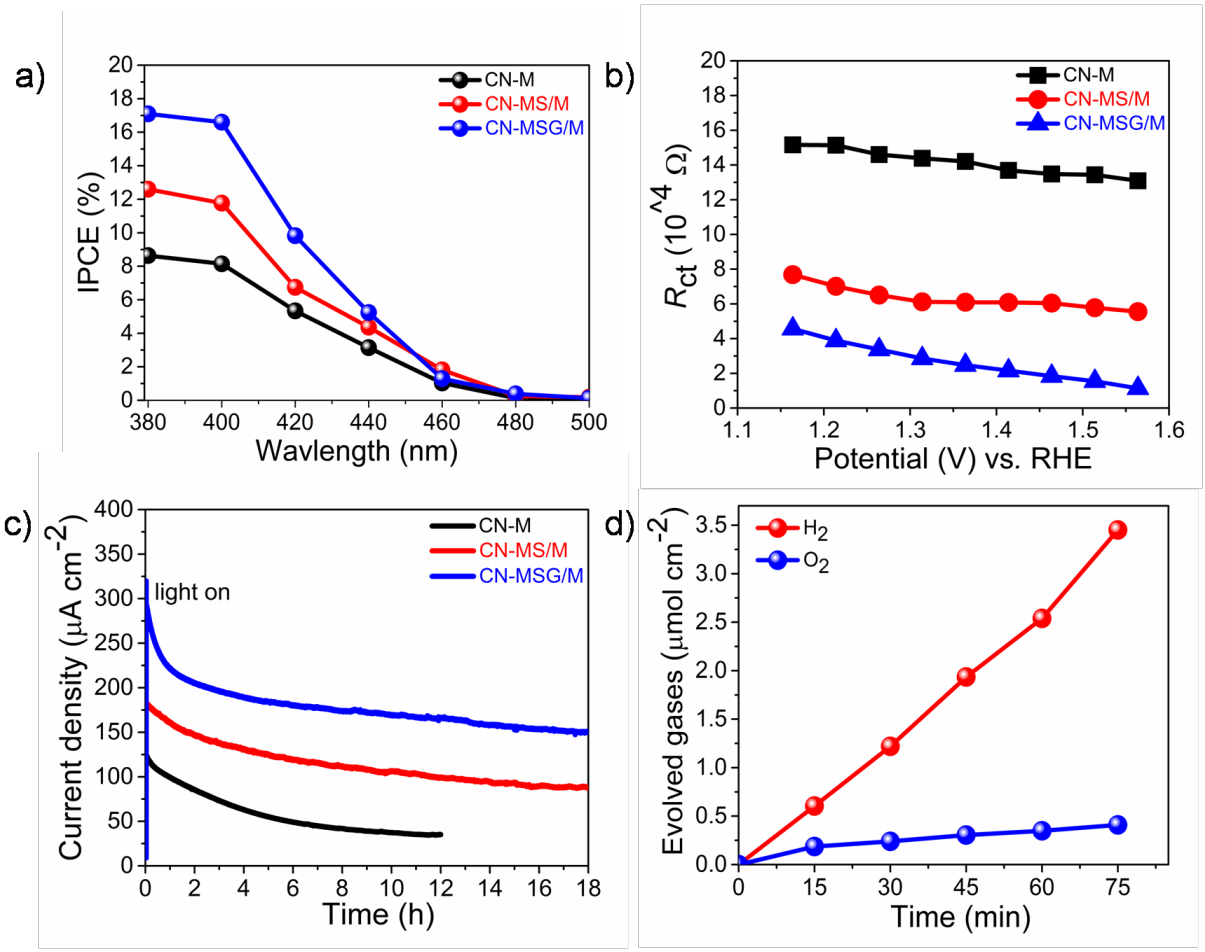

Figure 5. a) Incident photon-to-current conversion efficiency (IPCE) of CN electrodes at different wavelengths in 0.1 M KOH at 1.23 V vs. RHE. b) Charge transfer resistance (R_{ct}) of the CN electrodes at different applied potentials. c) Photocurrents of CN electrodes at 1.23 V vs. RHE in 0.1 M KOH aqueous solution during 18 h of continuous 1-sun illumination. d) Evolution of H_2 and O_2 measured by GC.

The photocurrent density is relatively stable after the initial decay; namely, after 2 h, a density decay of 40% is observed in the photocurrent of CN-MSG/M (Figure 5c). Nevertheless, after 18 h, only an additional 30% decay is observed, resulting in a photocurrent density of 150 μA cm^{-2} (a total decay of 44% after 18 h). Hence, the overall results prove the improvement in the stability of the sulfur- and rGO-modified CN films, presumably thanks to improved light absorption, enhanced electronic conductivity, and photo-oxidation ability. Post-characterization measurements after the long-term stability test indicate no significant structural changes (Figures S38–S40).

Another advantage of the new CN electrode is its stability over a wide pH range. To verify this, photocurrent densities were measured (Figure S41) in a strong acid (0.5 M H_2SO_4, pH 0.27) and in a neutral solution (0.5 M Na_2SO_4, pH 6.27). Despite the sluggish oxidation reaction at low pH, the photocurrent density shown by CN-MSG/M reached *ca*. 220 μA cm^{-2} (at 1.23 V vs. RHE) in the strongly acidic medium, while in the neutral solution, a photocurrent of ~200 μA cm^{-2} was obtained, alongside good stability. Moreover, LSV curves upon on/off illumination cycles of CN-MSG/M in 0.5 M Na_2SO_4 solution also showed a stable photocurrent with a very low onset potential (Figure S42a), as further confirmed by a continuous 18 h chronoamperometry, where only a 22% decay was observed (Figure S42b). We have performed simultaneous measurements of photocurrent and hydrogen (H_2) and oxygen (O_2) gas evolution measurements in 0.1 M KOH at 1.23 V vs. RHE (Figure 5d). The calculated Faradaic efficiency (Figure S43)[9,38] of CN-MSG/M photoanode for H_2 gas was ~60%, whereas for O_2, it was 28.7%, which dropped to 14.2% after longer irradiation times. Herein, Faradaic efficiency losses for O_2 evolution ultimately give non-stoichiometric proportion of H_2 and O_2 (Figure 5d), probably owing to partial photo-corrosion during water oxidation.[39] Additionally, the H_2 and O_2

were produced also in a phosphate buffer solution (0.1 M; pH 7 at 1.23 V vs. RHE) (Figure S44). The PEC H_2 generation in the presence of 10% (v/v) TEOA in 0.1 M KOH was analyzed by gas chromatography (GC) (Figure S45a). CN-MSG/M exhibited a constant H_2 generation rate (1.01 mmol g^{-1} h^{-1} after 3 h). The high rate of H_2 production demonstrated that the photoexcited electrons can easily be transferred from the photoanode to reduce water to H_2 (Figure S45b). The overall Faradaic efficiency for CN-MS/M and CN-MSG/M reached values of 57.9% and 72% (after 3 h), respectively.

In this work, we have reported the design of a carbon nitride electrode with excellent charge-separation, high electronic conductivity, and remarkable hole extraction efficiency. To this end, we utilized several complementary approaches that result in the growth of tightly-packed CN layers on top of rGO. The ordered CN layers configuration promotes the hole extraction efficiency up to 50% over a wide potential range, while the rGO enables larger electrons diffusion length. Moreover, further management of the electronic structure was achieved by forming a type-II heterojunction by growing a second CN layer *via* thermal vapor condensation. As a result, the new CN electrodes display excellent PEC performance, reaching up to 270 μA cm^{-2} in a 0.1 M KOH solution at 1.23 V vs. RHE, extremely low onset potential (~0.0012 V), as well as long-term stability, up to 18 h.

ASSOCIATED CONTENT

Supporting Information. The Supporting Information is available free of charge on the ACS Publications website.

Detailed materials and experimental methods, DFT calculations, UV–vis, FTIR, and XPS spectra, electrode fabrication process, additional EM characterization, XRD, BET, PEC measurements, GC measurements for H_2 and O_2 evolution, and Nyquist plots.

AUTHOR INFORMATION

Corresponding Author

* Email: mennysh@bgu.ac.il

ORCID iD

Neeta Karjule: 0000-0002-2664-5910

Jesús Bario: 0000-0002-4147-2667

Lidan Xing: 0000-0002-3642-7204

Michael Volokh: 0000-0001-8510-9336

Menny shalom: 0000-0002-4506-4177

Author Contributions

The manuscript was written through contributions of all authors. All authors have given approval to the final version of the manuscript.

Funding Sources

This project has received funding from the European Research Council (ERC) under the European Union's Horizon 2020 research and innovation programme (grant agreement No. [849068]). This work was also partially supported by the Israel Science Foundation (ISF), grant No. 1161/17 and ISF-NSFC grant No. 2969/19.

ACKNOWLEDGMENT

The authors thank Adi Azoulay, Jonathan Tzadikov, and Liel Abisdris for help with material characterization and Dr. Alexander Upcher for assistance with TEM analysis. We thank Dr. Chabanne for fruitful discussion.

REFERENCES

(1) Abe, R. Recent Progress on Photocatalytic and Photoelectrochemical Water Splitting under Visible Light Irradiation. *J. Photochem. Photobiol. C Photochem. Rev.* **2010,** *11*, 179–209.

(2) Otep, S.; Michinobu, T.; Zhang, Q. Pure Organic Semiconductor-Based Photoelectrodes for Water Splitting. *Sol. RRL* **2019,** 1900395.

(3) Zhang, Y.; Antonietti, M. Photocurrent Generation by Polymeric Carbon Nitride Solids: An Initial Step towards a Novel Photovoltaic System. *Chem. Asian J.* **2010,** *5*, 1307–1311.

(4) Xiong, W.; Huang, F.; Zhang, R.-Q. Recent Developments in Carbon Nitride Based Films for Photoelectrochemical Water Splitting. *Sustain. Energy Fuels* **2020,** *4*, 485–503.

(5) Safaei, J.; Mohamed, N. A.; Noh, M. F. M.; Soh, M. F.; Ludin, N. A.; Ibrahim, M. A.; Isahak, W. N. R. W.; Teridi, M. A. M. Graphitic Carbon Nitride (g-C_3N_4) Electrodes for Energy Conversion and Storage: A Review on Photoelectrochemical Water Splitting, Solar Cells and Supercapacitors. *J. Mater. Chem. A* **2018,** *6*, 22346–22380.

(6) Volokh, M.; Peng, G.; Barrio, J.; Shalom, M. Carbon Nitride Materials for Water Splitting Photoelectrochemical Cells. *Angew. Chem. Int. Ed.* **2019,** *58*, 6138–6151.

(7) Ruan, Q.; Bayazit, M. K.; Kiran, V.; Xie, J.; Wang, Y.; Tang, J. Key Factors Affecting Photoelectrochemical Performance of g-C_3N_4 Polymer Films. *Chem. Commun.* **2019,** *55*, 7191–7194.

(8) Zhao, T.; Zhou, Q.; Lv, Y.; Han, D.; Wu, K.; Zhao, L.; Shen, Y.; Liu, S.; Zhang, Y. Ultrafast Condensation of Carbon Nitride on Electrodes with Exceptional Boosted Photocurrent and Electrochemiluminescence. *Angew. Chem. Int. Ed.* **2020,** *59*, 1139–1143.

(9) Ye, K.-H.; Li, H.; Huang, D.; Xiao, S.; Qiu, W.; Li, M.; Hu, Y.; Mai, W.; Ji, H.; Yang, S. Enhancing Photoelectrochemical Water Splitting by Combining Work Function Tuning and Heterojunction Engineering. *Nat. Commun.* **2019,** *10*, 3687.

(10) Bian, J.; Xi, L.; Li, J.; Xiong, Z.; Huang, C.; Lange, K. M.; Tang, J.; Shalom, M.; Zhang, R. Q. C=C π Bond Modified Graphitic Carbon Nitride Films for Enhanced Photoelectrochemical Cell Performance. *Chem. Asian J.* **2017,** *12*, 1005–1012.

(11) Khan, M. S.; Zhang, F.; Osada, M.; Mao, S. S.; Shen, S. Graphitic Carbon Nitride-Based Low-Dimensional Heterostructures for Photocatalytic Applications. *Sol. RRL* **2019**, 1900435.

(12) Rahman, M. Z.; Davey, K.; Qiao, S. -Z. Carbon, Nitrogen and Phosphorus Containing Metal-Free Photocatalysts for Hydrogen Production: Progress and Challenges. *J. Mater. Chem. A* **2018,** *6*, 1305–1322.

(13) Li, X.-H.; Antonietti, M. Metal Nanoparticles at Mesoporous N-doped Carbons and Carbon Nitrides: Functional Mott–Schottky Heterojunctions for Catalysis. *Chem. Soc. Rev.* **2013,** *42*, 6593–6604.

(14) Zhang, Y.; Xia, B.; Ran, J.; Davey, K.; Qiao, S. Z. Atomic-Level Reactive Sites for Semiconductor-Based Photocatalytic CO_2 Reduction. *Adv. Energy Mater.* **2020,** *10*, 1903879.

(15) Barrio, J.; Mateo, D.; Albero, J.; García, H.; Shalom, M. A Heterogeneous Carbon Nitride–Nickel Photocatalyst for Efficient Low-Temperature CO_2 Methanation. *Adv. Energy Mater.* **2019,** *9*, 1902738.

(16) Liu, J.; Liu, Y.; Liu, N.; Han, Y.; Zhang, X.; Huang, H.; Lifshitz, Y.; Lee, S.-T.; Zhong, J.; Kang, Z. Metal-Free Efficient Photocatalyst for Stable Visible Water Splitting via a Two-Electron Pathway. *Science* **2015,** *347*, 970–974.

(17) Peng, G.; Qin, J.; Volokh, M.; Liu, C.; Shalom, M. Graphene Oxide in Carbon Nitride: From Easily Processed Precursors to a Composite Material with Enhanced Photoelectrochemical Activity and Long-Term stability. *J. Mater. Chem. A* **2019,** *7*, 11718–11723.

(18) Karjule, N.; Barrio, J.; Tzadikov, J.; Shalom, M. Electronic Structure Engineering of Carbon Nitride Materials Using Polycyclic Aromatic Hydrocarbons. *Chem. Eur. J.* **2020**, *26*, 1–8.

(19) Bian, J.; Xi, L.; Huang, C.; Lange, K. M.; Zhang, R. Q.; Shalom, M. Efficiency Enhancement of Carbon Nitride Photoelectrochemical Cells via Tailored Monomers Design. *Adv. Energy Mater.* **2016,** *6*, 1600263.

(20) Karjule, N.; Phatake, R.; Volokh, M.; Hod, I.; Shalom, M. Solution-Processable Carbon Nitride Polymers for Photoelectrochemical Applications. *Small Methods* **2019,** *3*, 1900401.

(21) Li, M.; Bai, Z.; Li, Y.; Ma, L.; Dai, A.; Wang, X.; Luo, D.; Wu, T.; Liu, P.; Yang, L.; Amine, K.; Chen, Z.; Lu, J. Electrochemically Primed Functional Redox Mediator Generator from the Decomposition of Solid State Electrolyte. *Nat. Commun.* **2019,** *10*, 1890.

(22) Merschjann, C.; Tschierlei, S.; Tyborski, T.; Kailasam, K.; Orthmann, S.; Hollmann, D.; Schedel-Niedrig, T.; Thomas, A.; Lochbrunner, S. Complementing Graphenes: 1D

Interplanar Charge Transport in Polymeric Graphitic Carbon Nitrides. *Adv. Mater.* **2015,** *27*, 7993–7999.

(23) Luan, P.; Meng, Q.; Wu, J.; Li, Q.; Zhang, X.; Zhang, Y.; O'Dell, L. A.; Raga, S. R.; Pringle, J.; Griffith, J. C. Unique Layer-Doping-Induced Regulation of Charge Behavior in Metal-Free Carbon Nitride Photoanodes for Enhanced Performance. *ChemSusChem* **2020**, *13*, 328–333.

(24) Peng, G.; Albero, J.; Garcia, H.; Shalom, M. A Water-Splitting Carbon Nitride Photoelectrochemical Cell with Efficient Charge Separation and Remarkably Low Onset Potential. *Angew. Chem. Int. Ed.* **2018,** *57*, 15807–15811.

(25) Peng, G.; Xing, L.; Barrio, J.; Volokh, M.; Shalom, M. A General Synthesis of Porous Carbon Nitride Films with Tunable Surface Area and Photophysical Properties. *Angew. Chem. Int. Ed.* **2018,** *57*, 1186–1192.

(26) Barrio, J.; Shalom, M. Rational Design of Carbon Nitride Materials by Supramolecular Preorganization of Monomers. *ChemCatChem* **2018,** *10*, 5573–5586.

(27) Karjule, N.; Barrio, J.; Tashakory, A.; Shalom, M. Bismuthiol-Mediated Synthesis of Ordered Carbon Nitride Nanosheets with Enhanced Photocatalytic Performance. *Sol. RRL* **2020**, 2000017.

(28) Sengupta, I.; Chakraborty, S.; Talukdar, M.; Pal, S. K.; Chakraborty, S. Thermal Reduction of Graphene Oxide: How Temperature Influences Purity. *J. Mater. Res.* **2018,** *33*, 4113–4122.

(29) Ong, W.-J.; Tan, L.-L.; Chai, S.-P.; Yong, S.-T.; Mohamed, A. R. Surface Charge Modification via Protonation of Graphitic Carbon Nitride (g-C_3N_4) for Electrostatic Self-Assembly Construction of 2D/2D Reduced Graphene Oxide (rGO)/g-C_3N_4 Nanostructures Toward Enhanced Photocatalytic Reduction of Carbon Dioxide to Methane. *Nano Energy* **2015,** *13*, 757–770.

(30) Ran, J.; Qu, J.; Zhang, H.; Wen, T.; Wang, H.; Chen, S.; Song, L.; Zhang, X.; Jing, L.; Zheng, R.; Qiao, S. Z. 2D Metal Organic Framework Nanosheet: A Universal Platform Promoting Highly Efficient Visible-Light-Induced Hydrogen Production. *Adv. Energy Mater*. **2019,** *9*, 1803402.

(31) Ran, J.; Zhu, B.; Qiao, S. Z. Phosphorene Co-catalyst Advancing Highly Efficient Visible-Light Photocatalytic Hydrogen Production. *Angew. Chem. Int. Ed*. **2017,** *56*, 10373–10377.

(32) Hong, J.; Xia, X.; Wang, Y.; Xu, R. Mesoporous Carbon Nitride with in Situ Sulfur Doping for Enhanced Photocatalytic Hydrogen Evolution from Water under Visible Light. *J. Mater. Chem,* **2012,** *22*, 15006–15012.

(33) Zhang, J.; Sun, J.; Maeda, K.; Domen, K.; Liu, P.; Antonietti, M.; Fu, X.; Wang, X. Sulfur-Mediated Synthesis of Carbon Nitride: Band-Gap Engineering and Improved Functions for Photocatalysis. *Energy Environ. Sci*. **2011,** *4*, 675–678.

(34) Song, J.-Y.; Kang, H.-J.; Won, J. C.; Kim, Y. H.; Jun, Y.-S.; Jeong, H. S. The True Liquid Crystal Phases of 2D Polymeric Carbon Nitride and Macroscopic Assembled Fibers. *Mater. Horizons* **2019,** *6*, 1726–1732.

(35) Klotz, D.; Grave, D. A.; Rothschild, A. Accurate Determination of the Charge Transfer Efficiency of Photoanodes for Solar Water Splitting. *Phys. Chem. Chem. Phys.* **2017,** *19*, 20383-20392.

(36) Alam, K. M.; Kumar, P.; Kar, P.; Thakur, U. K.; Zeng, S.; Cui, K.; Shankar, K. Enhanced Charge Separation in g-C_3N_4–BiOI Heterostructures for Visible Light Driven Photoelectrochemical Water Splitting. *Nanoscale Adv*. **2019,** *1*, 1460–1471.

(37) Ruan, Q.; Luo, W.; Xie, J.; Wang, Y.; Liu, X.; Bai, Z.; Carmalt, C. J.; Tang, J. A Nanojunction Polymer Photoelectrode for Efficient Charge Transport and Separation. *Angew. Chem. Int. Ed*. **2017,** *56*, 8221–8225.

(38) Kim, W.; Tachikawa, T.; Monllor-Satoca, D.; Kim, H.-i.; Majima, T.; Choi, W. Promoting Water Photooxidation on Transparent WO_3 Thin Films Using an Alumina Overlayer. *Energy Environ. Sci*. **2013,** *6*, 3732–3739.

(39) Wang, L.; Mitoraj, D.; Turner, S.; Khavryuchenko, O. V.; Jacob, T.; Hocking, R. K.; Beranek, R. Ultrasmall CoO(OH)x Nanoparticles As a Highly Efficient "True" Cocatalyst in Porous Photoanodes for Water Splitting. *ACS Catal*. **2017,** *7*, 4759–4767.

Table of Contents

Highly Efficient Polymeric Carbon Nitride Photoanode with Excellent Electron Diffusion Length and Hole Extraction Properties

*Neeta Karjule,[a] Jesús Barrio,[a] Lidan Xing,[b] Michael Volokh[a] and Menny Shalom[a]**

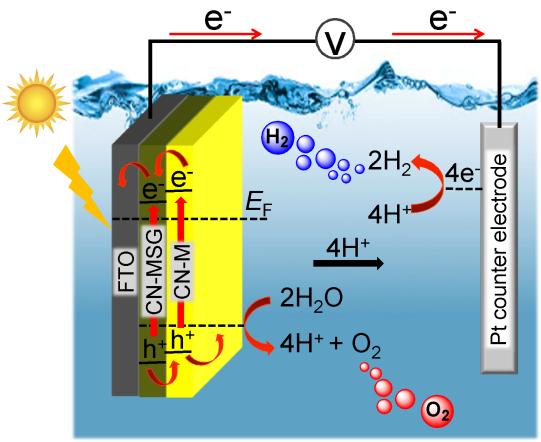

Supporting Information for

Highly Efficient Polymeric Carbon Nitride Photoanode with Excellent Electron Diffusion Length and Hole Extraction Properties

*Neeta Karjule,[a] Jesús Barrio,[a] Lidan Xing,[b] Michael Volokh[a] and Menny Shalom[a]**

[a]*Department of Chemistry and Ilse Katz Institute for Nanoscale Science and Technology, Ben-Gurion University of the Negev, Beer-Sheva 8410501, Israel*
[b]*School of Chemistry, South China Normal University, Guangzhou, 510006 China*

Corresponding Author. Email: mennysh@bgu.ac.il

Materials

All chemicals were purchased from commercial sources and used without further purification. Melamine (99%) was purchased from Sigma-Aldrich. Bismuthiol (1,3,4-thiadiazole-2,5-dithiol, (97%)) was purchased from Alfa Aesar. Dimethyl sulfoxide (DMSO, 99.90%) was purchased from Fisher Scientific. Ethylene glycol (EMSURE® Reag. Ph. Eur, Reag. USP) was purchased from Merck. Triethanolamine (99%) was purchased from Glentham Life Sciences. Nitric acid (HNO_3, 67–69 wt %, for trace metal analysis) was purchased from Fisher Chemical. Fluorine-doped tin oxide (FTO) coated glass (12–14 Ω sq^{-1}) was purchased from Xop Glass Company, Spain. De-ionized water (DI) was obtained from a Millipore Direct-Q® 3 water purification system (18.2 MΩ cm resistivity). Graphene oxide (GO, 0.4 wt %, >95%) aqueous suspension was purchased from University Wafer Inc. USA (C89/GOSD18004/D).

Characterization

Scanning electron microscopy (SEM) images of the supramolecular complex and CN were obtained using a JEOL JSM-7400F high-resolution SEM, equipped with a FEG

source, operated at 4.0 kV for imaging and at 12 kV for energy-dispersive spectroscopy (EDS) elemental mapping, and using a Thermo Scientific Noran SIX detection system. SEM samples were sputtered with Platinum (Pt) before analysis. UV-vis absorption spectra were measured on a Cary 100 spectrophotometer. Transmission electron microscopy (TEM) images were obtained from a Tecnai T12 G^2 TWIN microscope at an accelerating voltage of 120 kV. EDS analysis was performed using a JEOL JEM-2100F TEM operating at 200 kV equipped with a JED-2300T energy dispersive X-ray spectrometer. Scanning TEM (STEM) images were taken using a GATAN 806 HAADF STEM detector. The probe size during the analysis was set to 1 nm. JEOL Analytical Station software (v. 3.8.0.21) was used for the EDS data analysis. Fluorescence measurements were carried out on FluroMax®4 spectrofluorometer from Horiba Scientific. Fourier-transform infrared spectroscopy (FTIR) was performed on a Thermo Scientific Nicolet iS5 FTIR spectrometer (equipped with a Si ATR). X-ray photoelectron spectroscopy (XPS) was performed on a Thermo Fisher Scientific ESCALAB 250 using monochromated Kα X-rays (1486.6 eV). X-ray diffraction patterns (XRD) were obtained using a PANalytical's Empyrean diffractometer equipped with a position sensitive detector X'Celerator. Data was collected with a scanning time of ~7 min for 2θ ranging from 5° to 60° using Cu Kα radiation (λ = 1.54178 Å, 40 kV, 30 mA). Elemental analysis data for carbon, nitrogen, and hydrogen (CNH) was collected using a Thermo Scientific Flash Smart elemental analyzer OEA 2000. Samples for inductively-coupled plasma optical emission spectrometry (ICP-OES) were prepared by dissolution in concentrated nitric acid in a PTFE-lined autoclave at 180 °C for 8 h. Then, the prepared samples were analyzed using a Spectro ARCOS ICP-OES, FHX22 multi-view plasma instrument (radial configuration). Nitrogen-sorption measurements and Brunauer-Emmet-Teller (BET) specific surface area calculations were performed on a Quantachrome NOVAtouch NT LX^3 system. The thickness of CN films was measured by 3D laser confocal scanning microscope (LEXT OLS5000).

Experimental section

Synthesis of a supramolecular assembly of Melamine-Bismuthiol (MS)[1]

Equimolar amounts of a sulfur-containing monomer, bismuthiol (S), and melamine (M) were mixed in dimethylsulfoxide (DMSO) to form a hydrogen-bonded supramolecular framework (MS, Figures 1 and S1a).

In a typical synthesis, melamine (1.00 g, 7.93 mmol) was dissolved in 40 mL DMSO and an equimolar amount of bismuthiol (1,3,4-thiadiazole-2,5-dithiol) (1.19 g, 7.93 mmol) was dissolved in 10 mL DMSO. The melamine solution was kept at 60 °C and then mixed with bismuthiol under constant stirring for 10 min. The Melamine-bismuthiol (MS (DMSO)) supramolecular complex was obtained by precipitation through the addition of 150 mL of H_2O into the above solution. The mixture was filtered, washed with water, and then dried at 90 °C to get MS (DMSO) powder.

Melamine, MS, and MSG$_x$ film preparation

Melamine films (M) were prepared by grinding melamine powder (2.0 g) in 1.2 mL ethylene glycol until obtaining a viscous paste. For the preparation of MS films, supramolecular powders (1.0 g) were ground into fine slurries in ethylene glycol (3 mL). The obtained paste was doctor-bladed (with different numbers of scotch tape layers (L) in order to control the thickness) onto FTO to achieve a homogeneous coating, and subsequently dried at 90 °C on a hot plate, and finally transferred into a closed 16 mm-diameter glass test tube. (Note that all the FTO substrates were cleaned by a successive sonication in an aqueous soap solution (1 % w/v Alconox), then acetone and ethanol, and then dried before usage).

For the preparation of the Melamine-Bismuthiol-Graphene oxide (MSG$_x$) supramolecular paste, 1.0 g of the MS powder was blended thoroughly in 3 mL ethylene glycol with different amounts of 0.8 wt % graphene oxide (0.8 wt % GO suspension was prepared by concentrating commercial GO of 0.4 wt %) aqueous suspension (x = 0.25, 0.5, 0.75, and 1.0 mL) and the obtained paste was casted on FTO by the doctor-blade technique. The films were dried on a hot plate and transferred into a glass test tube.

Synthesis of a CN electrode

During the calcination process, two electrodes were kept in a 16 mm-diameter glass test tube. Additionally, 1.0 g of melamine powder was placed at the bottom of the test tube. The test tube was purged very carefully with nitrogen gas for 5 min and then covered with aluminium foil. Then, the samples were heated up to 550 °C at a ramp rate of 5 °C

min^{-1} and kept at 550 °C for 4 h under a flow of N_2 to get CN-MS/M and CN-MSG/M electrodes. Reference CN-M electrodes were prepared at the same heating conditions but without the addition of melamine powder inside the tubes.

Photoelectrochemical measurements

All electrochemical measurements were performed using a three-electrode system on an Autolab potentiostat (Metrohm, PGSTAT 101). A Pt-foil electrode (1 cm^2) and an Ag/AgCl (saturated KCl) electrode were used as the counter and reference electrodes, respectively. The electrolyte was either a 0.1 M KOH aqueous solution (pH ~13.1) or a 0.1 M KOH solution containing 10% (v/v) triethanolamine. All the potentials were converted to reversible hydrogen electrode (RHE) values using equation S1.

$$\textbf{Equation S1}.\ V_{RHE} = V_{Ag/AgCl} + 0.059 \cdot pH + 0.197$$

Photocurrents were measured at 1.23 V *vs.* RHE under the illumination of a solar simulator (Newport 300 W Xe arc lamp, equipped with an AM 1.5G and water filters) at a power density of 100 mW cm^{-2}, which was calibrated using a power meter (Model 919-P, Newport). The Nyquist plots and IPCE of the samples were measured using an Autolab potentiostat (Metrohm, PGSTAT 101). Incident photon-to-current conversion efficiency (IPCE) values were obtained using the equation S2:

$$\textbf{Equation S2}.\ \mathrm{IPCE}(\%) = \frac{J\ (\mathrm{A\ cm^{-2}}) \cdot 1240}{\lambda\ (\mathrm{nm}) \cdot I\ (\mathrm{W\ cm^{-2}})} \cdot 100\%$$

Where λ is the wavelength of the incident monochromic light, I is the incident illuminating power, J is the measured photocurrent density. The monochromic incident lights with wavelengths of 380 nm, 400 nm, 420 nm, 440 nm, 460 nm, 480 nm, and 500 nm were generated by coupling the solar simulator with the corresponding band pass filters (the band pass filters were purchased from Thorlabs; FB380-10, FB400-10, FB420-10, FB440-10, FB460-10, FB480-10, FB500-10). Nyquist plots of the samples were measured in the frequency range from 100 kHz to 10 mHz at different applied voltages. Mott–Schottky plots of CN were measured in 1.0 M Na_2SO_4 at a frequency of 2.0 kHz. Charge transfer efficiency (η_t, %) was calculated by dividing the photocurrent obtained in the absence of the hole scavenger by the photocurrent obtained in its presence. Long-term stability for all CN films was determined by monitoring the photocurrent density *vs.* time under constant illumination (at 1.23 V *vs*. RHE).

Hydrogen and oxygen evolution measurements

The amount of photogenerated H_2 and O_2 in the reactor headspace was analyzed using a gas chromatography (Agilent 7820A GC system) equipped with a thermal conductivity detector (TCD). Samples of gases were intermittently withdrawn every 15 min with an A-2 Luer lock gas syringe series purchased from VICI® precision sampling (Pressure-lok® precision analytical syringe). PEC cell compartments were thoroughly sealed with rubber septa and parafilm to prevent any gas leakage. Prior to any measurement, the electrolyte was purged with Ar for 30 min. The electrode was continuously held at 1.23 V (*vs*. RHE) under 1-sun illumination.

Density functional theory (DFT) calculations

All calculations were performed using the Gaussian 09 package. The equilibrium structures were optimized by B3LYP method in conjunction with the 6 311++G (d) basis set. To confirm each optimized stationary point, frequency analyses were done with the same basis set. DMSO was utilized in polarized continuum models (PCM) to investigate the role of solvent effects.

Figure S1. a) Schematic illustration of the formation of MS (melamine-bismuthiol) supramolecular assemblies. b) SEM image of the as-synthesized supramolecular MS (DMSO) assembly.

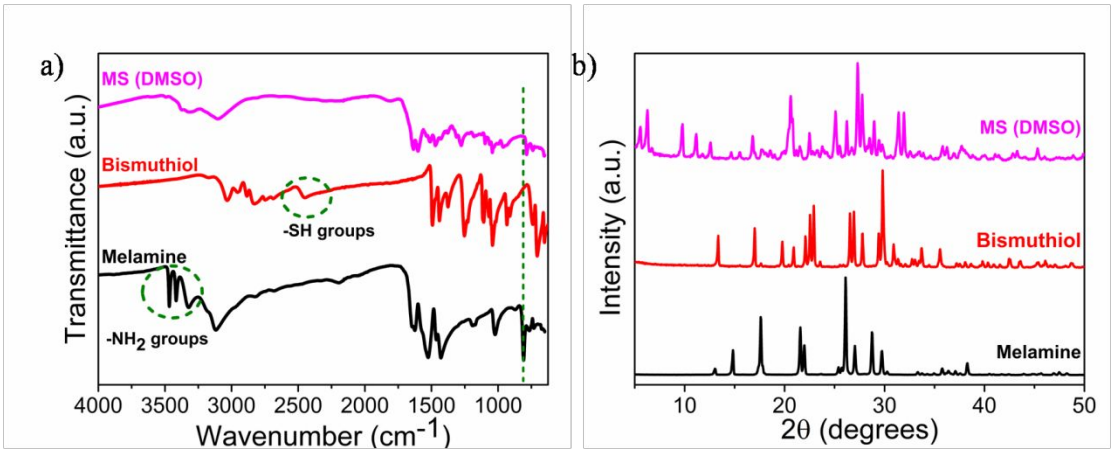

Figure S2. a) FTIR spectra and b) XRD patterns of the reactant monomers (melamine (black) and bismuthiol (red)) and their supramolecular complex (MS, prepared in DMSO (pink)).

The formation of a hydrogen-bonded supramolecular MS complex was confirmed by FTIR and powder XRD (Figure S2a and S2b, respectively). FTIR showed the disappearance of the stretching vibrations corresponding to the amine groups (νN–H) of melamine (at 3469 and 3414 cm^{-1}) and stretching vibrations of the thiol groups of bismuthiol (νS–H) (at 2400–2600 cm^{-1}). Additionally, the vibrations corresponding to the C–N heterocycles of the triazine ring and the bismuthiol moiety disappear and new peaks emerge at 1200–1600 cm^{-1} (Figure S2a). The formation of hydrogen bonds within the MS complex shifted the stretching vibration of triazine ring from 805 to 782 cm^{-1}. The XRD patterns display the formation of a new crystal structure, as observed in the appearance of an intense peak at low 2θ values (6.3°) corresponding to a repeating in-plane unit (Figure S2b), which confirms the formation of a new arrangement.

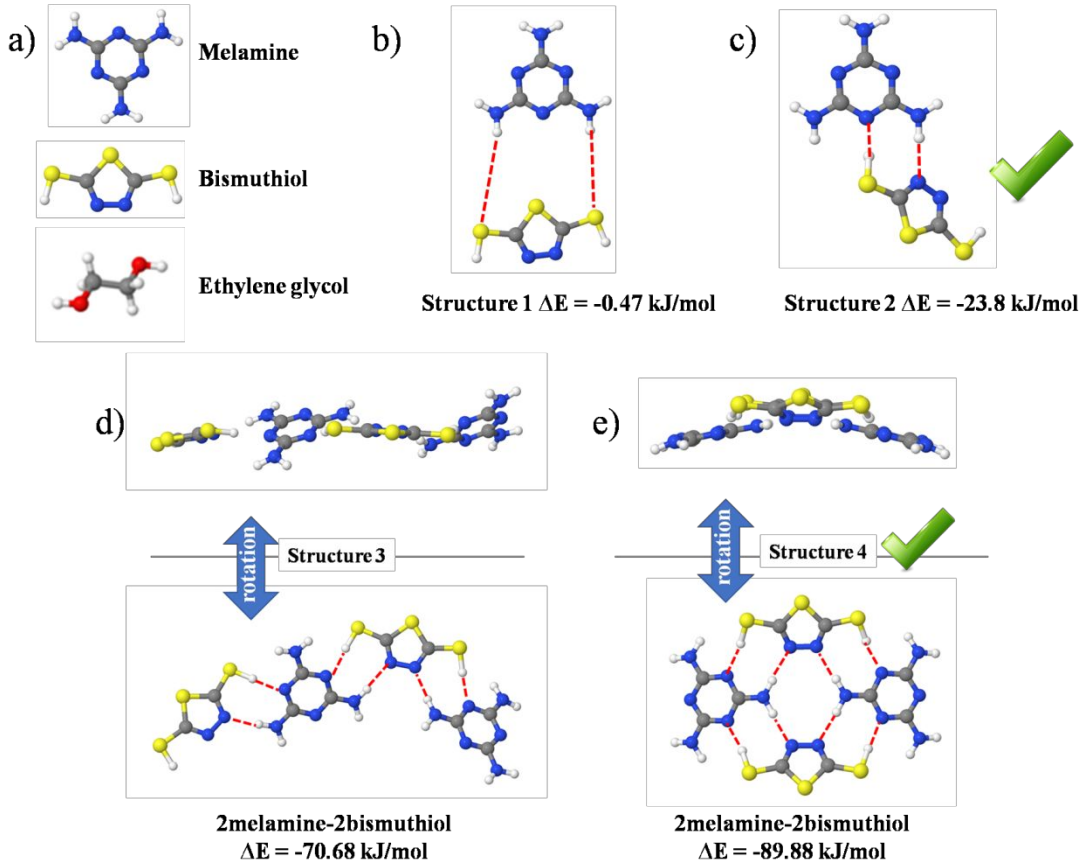

Figure S3. DFT simulation of the interaction energy between the melamine- bismuthiol supramolecular assembly (The interaction energy, ΔE, is labeled below each configuration).

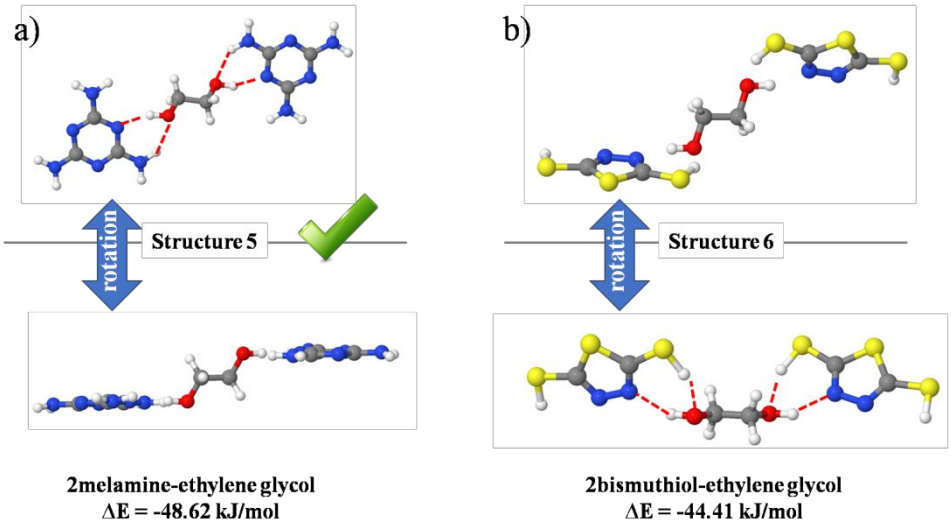

Figure S4. DFT simulation of the interaction between ethylene glycol (EG) with melamine-bismuthiol supramolecular assembly (The interaction energy, ΔE, is labeled below each configuration).

Density functional theory (DFT) was used to calculate the interaction energy (E_{int}) between the monomers, solvent and ethylene glycol (EG), in order to understand the molecular binding configuration. The calculated E_{int} between melamine and EG (-48.62 kJ/mol) is lower than between bismuthiol and EG (-44.41 kJ/mol), indicating that the EG would preferentially bind to melamine through two parallel hydrogen bonds (Figure 1c and Figure S4). Therefore, based on these calculations, we propose a molecular structure of supramolecular assemblies after the incorporation of EG (Figure S5).

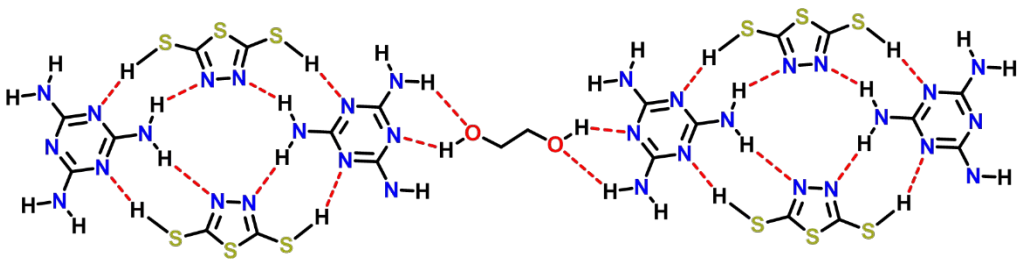

Figure S5. Possible supramolecular assembly structure after incorporating EG (based on DFT calculations).

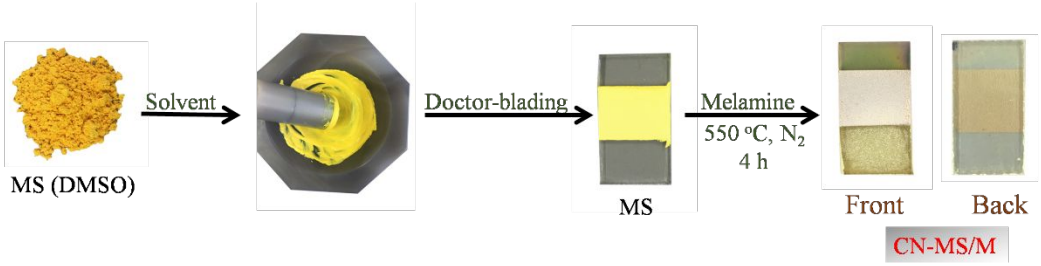

Figure S6. Digital images describing the synthetic procedure for the preparation of CN-MS/M electrodes (on FTO-coated glass substrates).

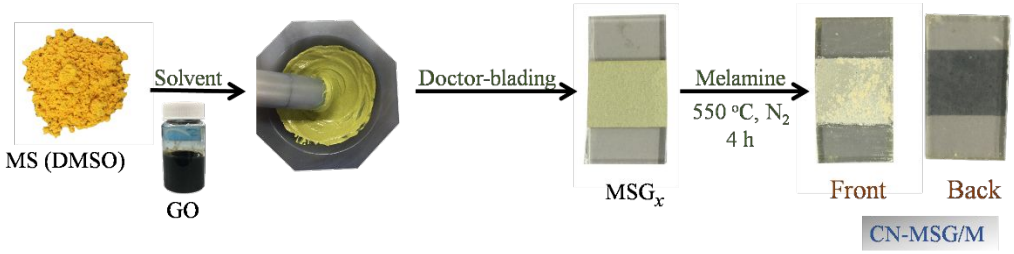

Figure S7. Digital images describing the synthetic procedure for the preparation of CN-MSG/M electrodes (on FTO-coated glass substrates).

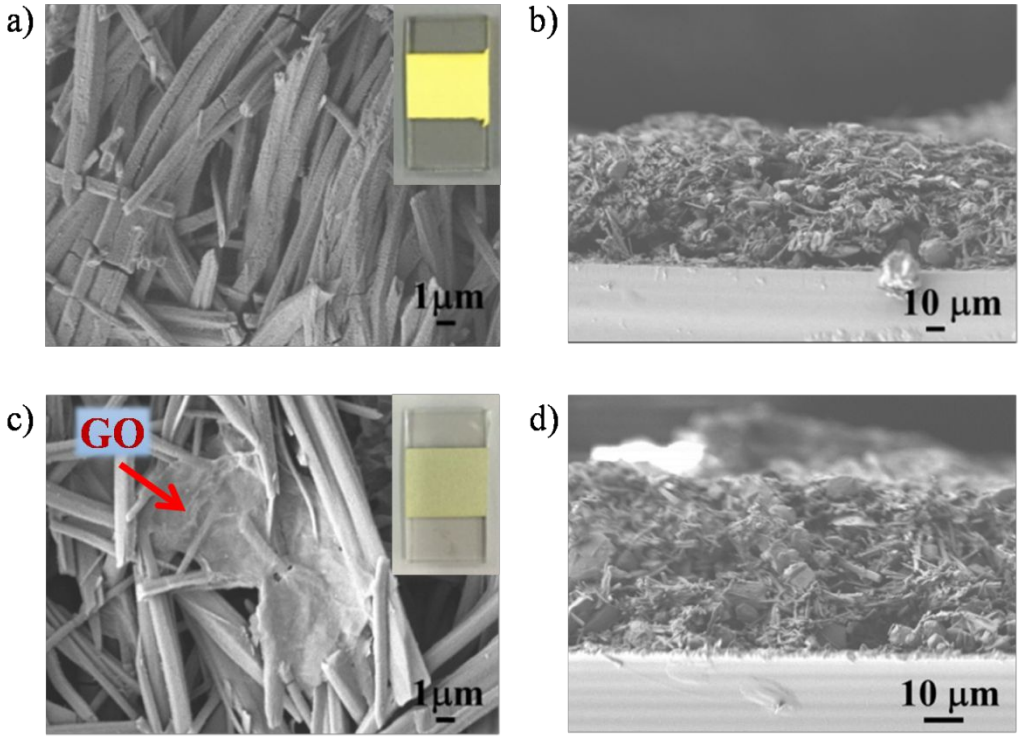

Figure S8. SEM images. a) top-view and b) cross-section of MS films (melamine-bismuthiol). c) top-view and d) cross-section of $MSG_{0.75}$ (melamine-bismuthiol-graphene oxide (GO)) films on FTO before calcination.

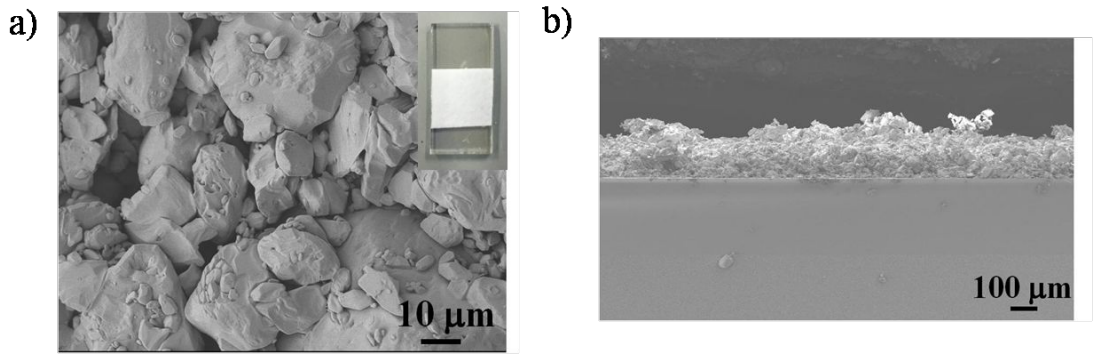

Figure S9. SEM images of a melamine film. a) top-view and b) cross-section (thickness is *ca.* 180 µm).

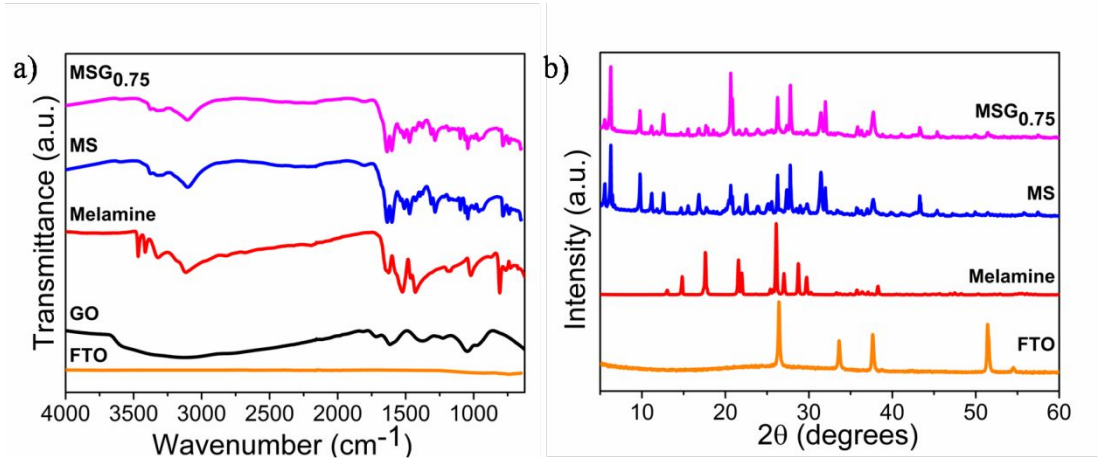

Figure S10. a) FTIR spectra and b) XRD patterns of melamine, MS, and $MSG_{0.75}$ films (on FTO-coated glass).

FTIR and XRD measurements confirm that the incorporation of GO neither affects the chemical nature of MS nor its crystal structure (Figure S10a–b).

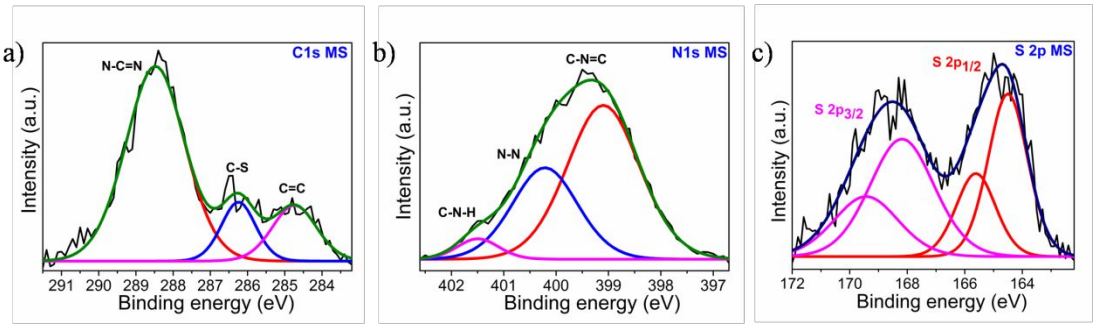

Figure S11. High-resolution XPS spectra of MS film. a) C1s, b) N1s, and c) S2p.

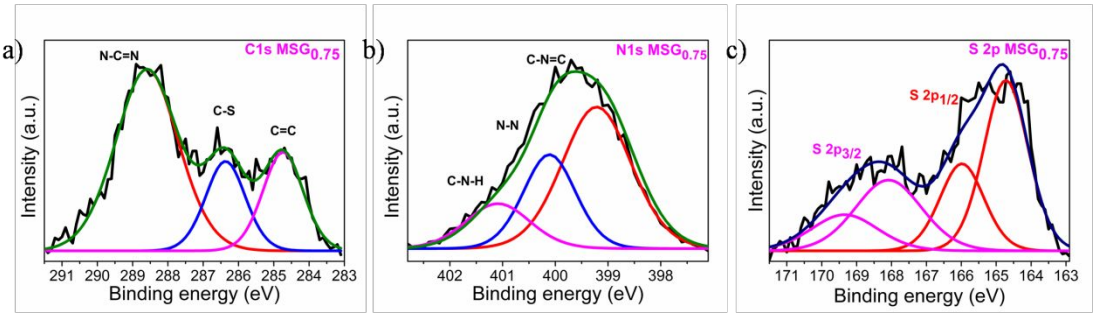

Figure S12. High-resolution XPS spectra of $MSG_{0.75}$ film. a) C1s, b) N1s, and c) S2p.

The C1s spectrum confirms the presence of C–S bonds at 286.2 eV, which proves the inclusion of bismuthiol molecules (Figures S11–S12). We note that in the $MSG_{0.75}$ electrode this contribution represents a higher area due to the synergistic contribution of the C–O bonds of GO. The peak at 288.5 eV corresponds to the C–N=C chemical species and the peak at 284.8 eV is attributed to C=C. In the N1s spectrum, the deconvoluted peaks at 399.1, 400.2, and 401.5 eV can be assigned to the C–N=C, N–N (nitrogen–nitrogen bonds of the bismuthiol moiety), and C–N–H, respectively. The high-resolution S2p spectra were deconvoluted into two peaks at 164.2 (C−S−C),[2] and 168.2 eV (–SH groups), which confirms the presence of bismuthiol moieties in the starting supramolecular films (Figures S11c–S12c).

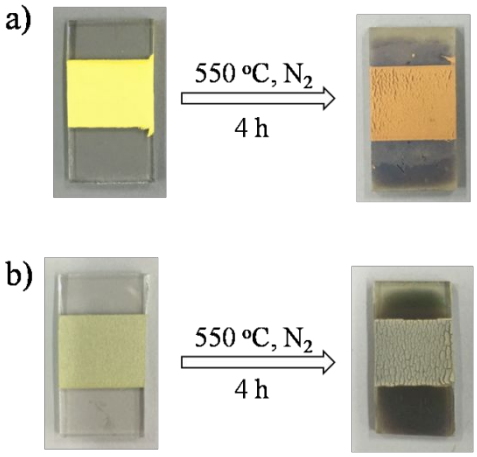

Figure S13. Digital images of a) CN-MS and b) CN-$MSG_{0.75}$ electrodes prepared without addition of melamine in the glass tube.

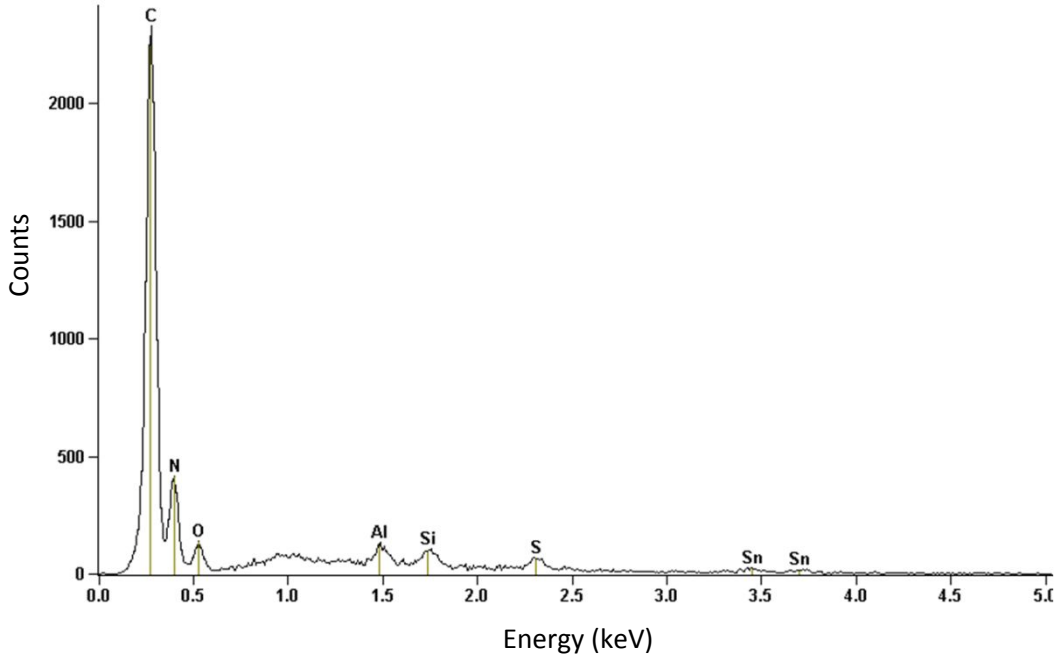

Figure S14. EDS spectrum for CN-$MSG_{0.75}$/M (or CN-MSG/M) film.

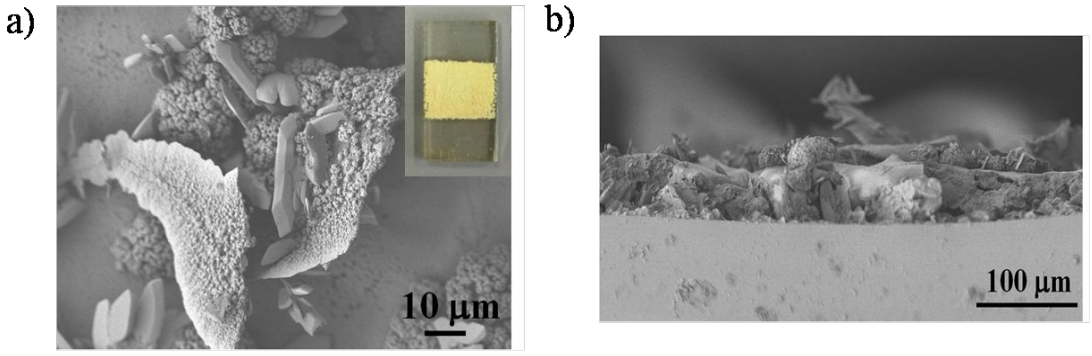

Figure S15. SEM images of CN-M electrodes. a) top-view and b) cross-section.

Table S1. Elemental analysis of films and CN electrodes (powder scratched from FTO for analysis)

Sample	Carbon /at. %	Nitrogen /at. %	Hydrogen /at. %	C/N	Sulfur /at. %
M	19.97	40.13	39.91	0.50	—
CN-M	32.77	49.33	17.90	0.66	—
MS	21.58	35.21	35.13	0.61	8.07
CN-MS/M	29.46	45.8	23.52	0.64	0.22
MSG	26.52	34.23	28.54	0.77	10.70
CN-$MSG_{0.75}$/M	34.27	48.16	17.46	0.71	0.19

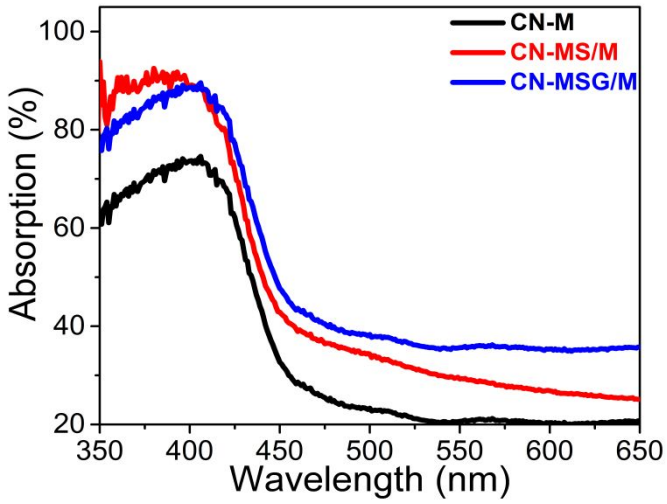

Figure S16. UV-vis spectra of CN electrodes.

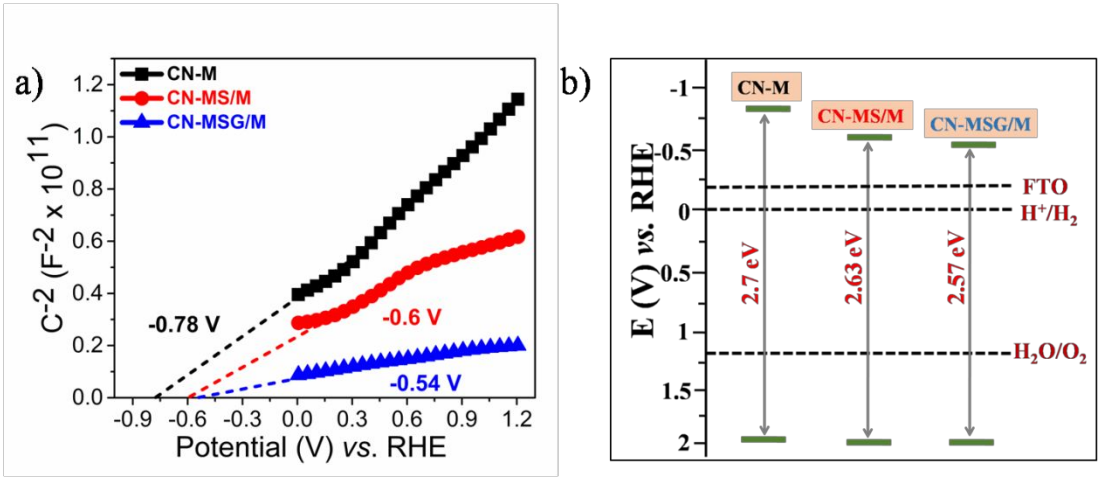

Figure S17. (a) Mott-Schottky plots. (b) Proposed energy diagram of the CN-M, CN-MS/M, and CN-MSG/M electrodes.

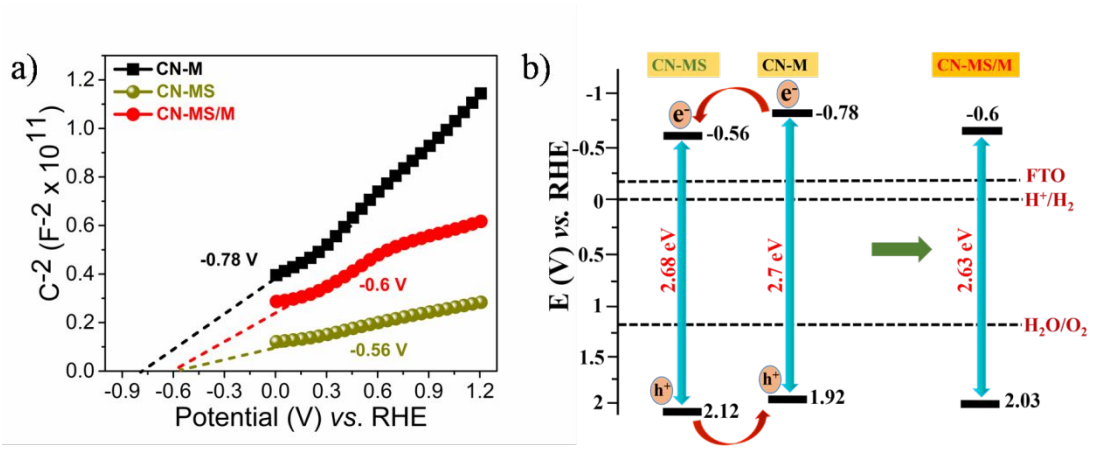

Figure S18. a) Mott-Schottky plots for CN-M, CN-MS, and CN-MS/M. (b) Proposed energy levels diagram for the heterojunction formation between CN-M and CN-MS.

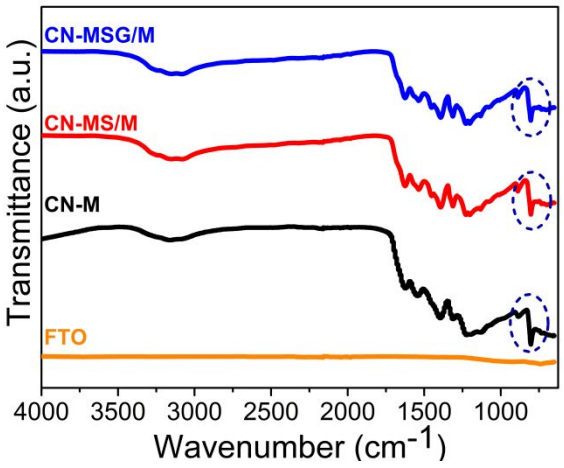

Figure S19. FTIR spectra of the different CN electrodes.

The broad peak at 3150 cm^{-1} belongs to free amine groups at the surface, the stretching bands of the CN heterocycles can be observed between 1200−1600 cm^{-1}, and the characteristic breathing mode of triazine rings appears at 800 cm^{-1} (Figure S19).

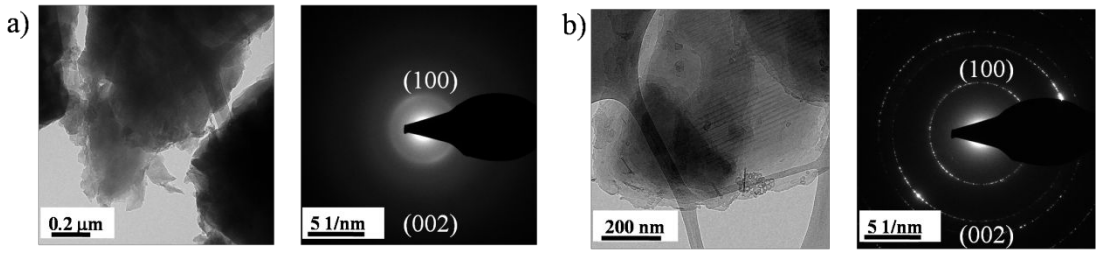

Figure S20. TEM images with the corresponding SAED patterns. a) CN-M, b) CN-MS/M. In order to prepare optimal samples for TEM imaging, some powder was scratched from the CN electrodes.

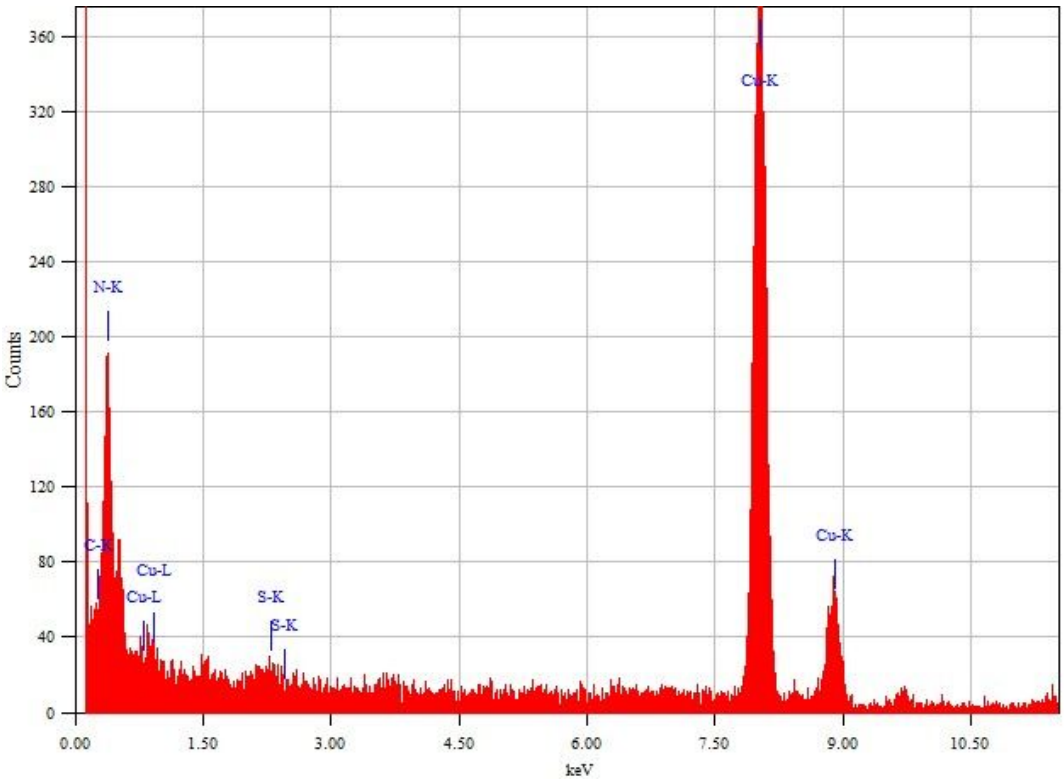

Figure S21. EDS spectrum of CN-MSG/M (measured on a copper TEM grid).

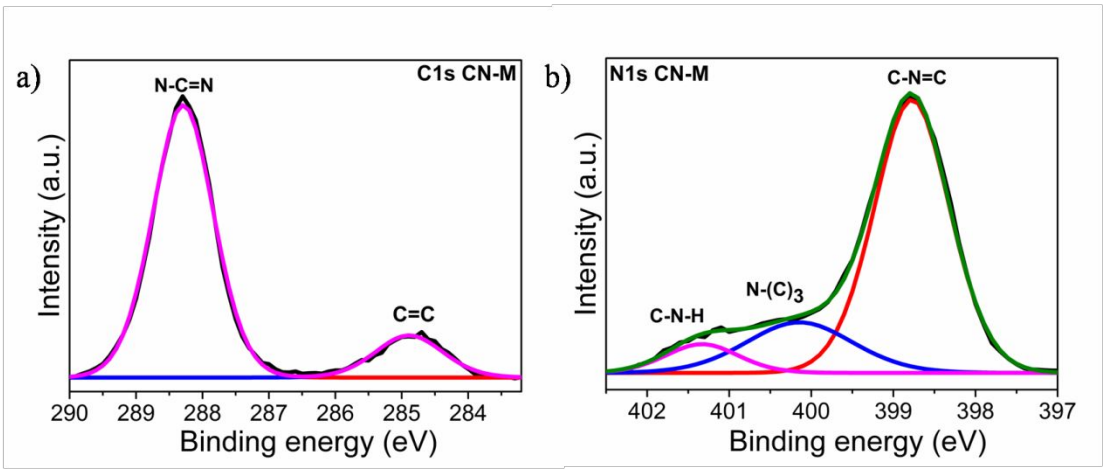

Figure S22. High-resolution XPS spectra. a) C1s and b) N1s of CN-M electrode.

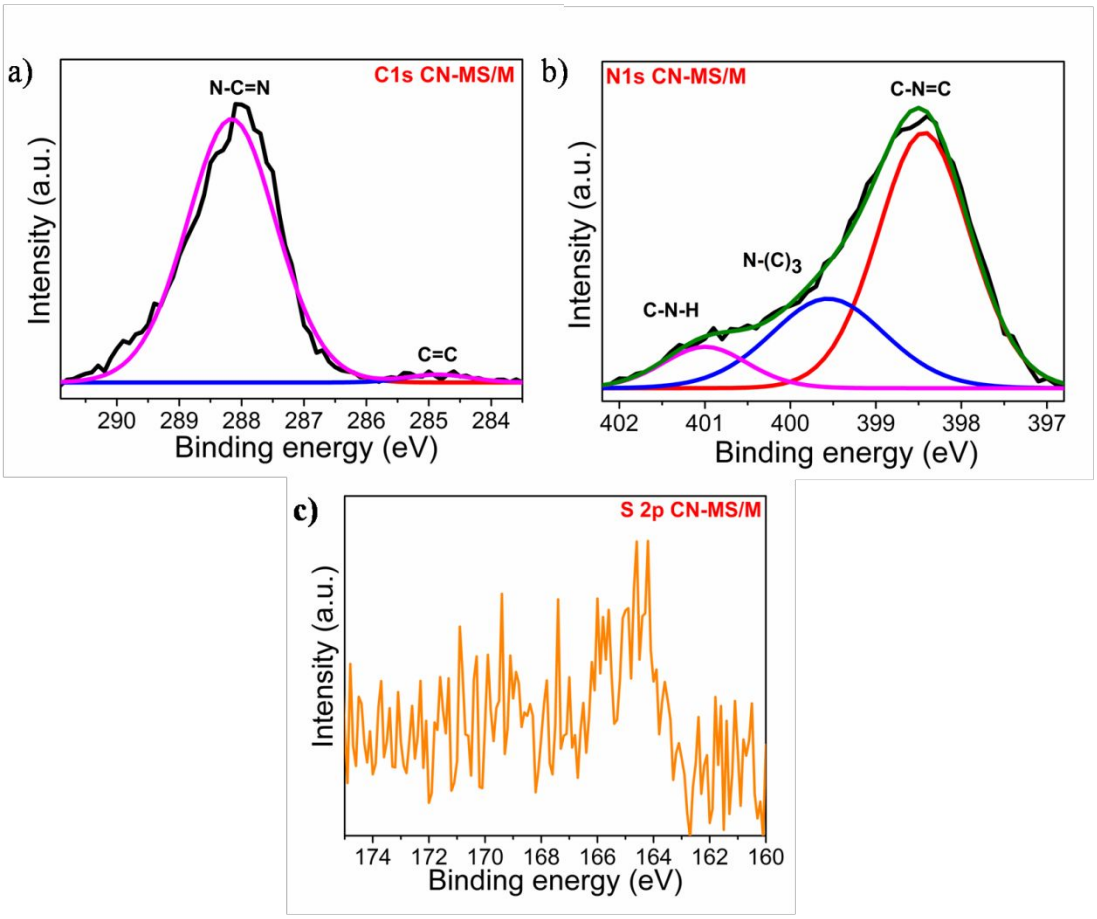

Figure S23. High-resolution XPS spectra. a) C1s, b) N1s, and c) S2p of CN-MS/M electrode.

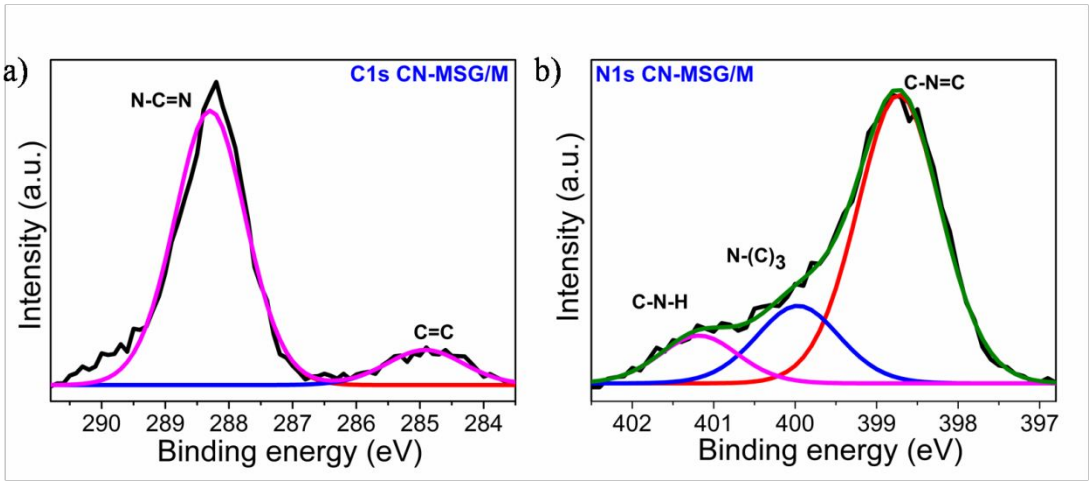

Figure S24. High-resolution XPS spectra. a) C1s and b) N1s of CN-MSG/M electrode.

In the C1s spectrum, the strong peak at 288.3 eV is attributed to C–N=C moieties and the binding energy at 284.9 eV corresponds to C–C bonds. The N1s spectrum indicated three peaks centered at 398.8, 400.2, and 401.4 eV, which are

ascribed to C–N=C bonds, tertiary nitrogen N–$(C)_3$ groups, and C–N–H bonds, respectively (Figure S22-24). In addition, the XPS spectrum for S2p revealed a weak chemical contribution at 164 eV, which may be attributed to trace amounts of sulfur covalently bonded to C, replacing N atoms in the heptazine unit (Figure S23c).

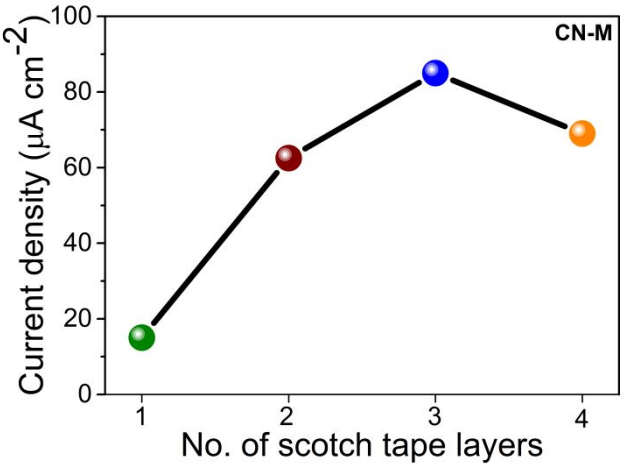

Figure S25. Photocurrent densities of CN-M electrodes of variable thickness in 0.1 M KOH (at 1.23 V *vs.* RHE) prepared by using 1–4 scotch tape layers during the preparation.

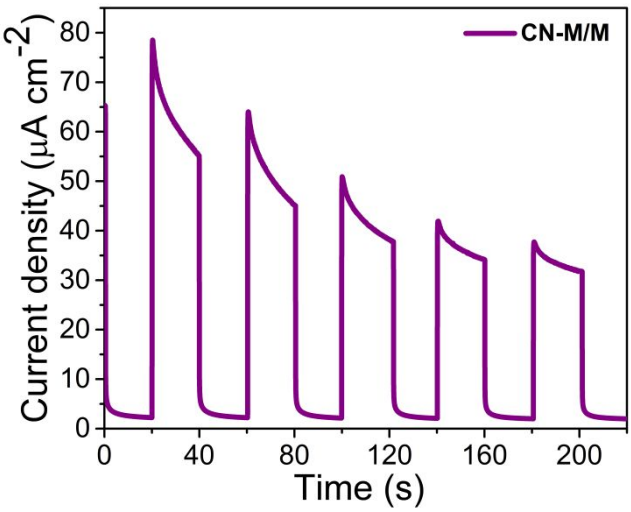

Figure S26. Photocurrent density of CN-M/M in 0.1 M KOH (at 1.23 V *vs.* RHE).

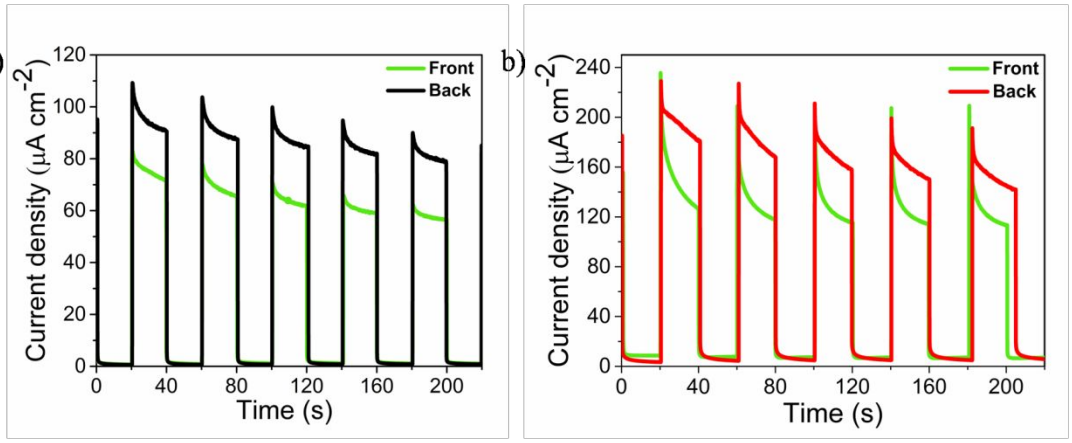

Figure S27. Photocurrent densities upon illumination from front- and back-side. a) CN-M and b) CN-MS/M electrodes at 1.23 V *vs*. RHE in 0.1 M KOH.

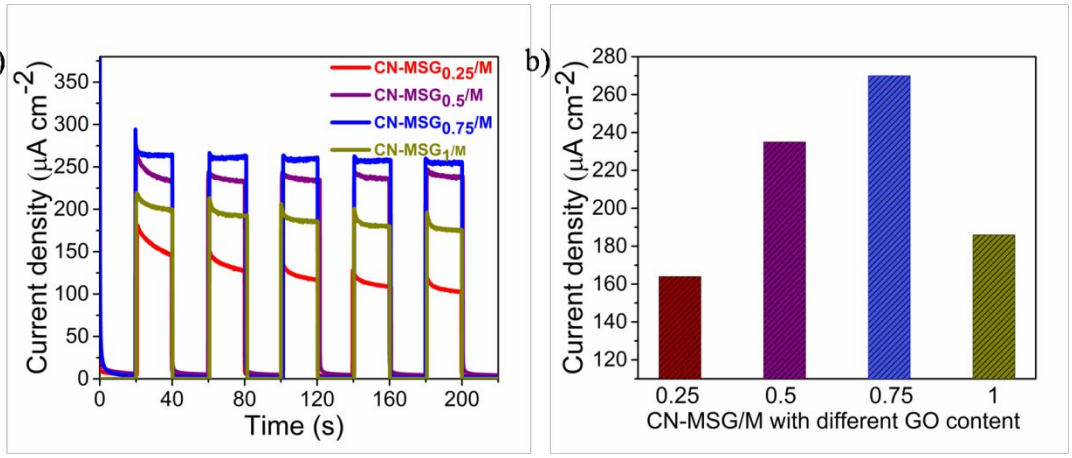

Figure S28. a) Photocurrent densities of CN-MSG$_x$/M (x = 0.25–1 mL). b) Photocurrent–GO content relationship for CN-MSG/M electrodes.

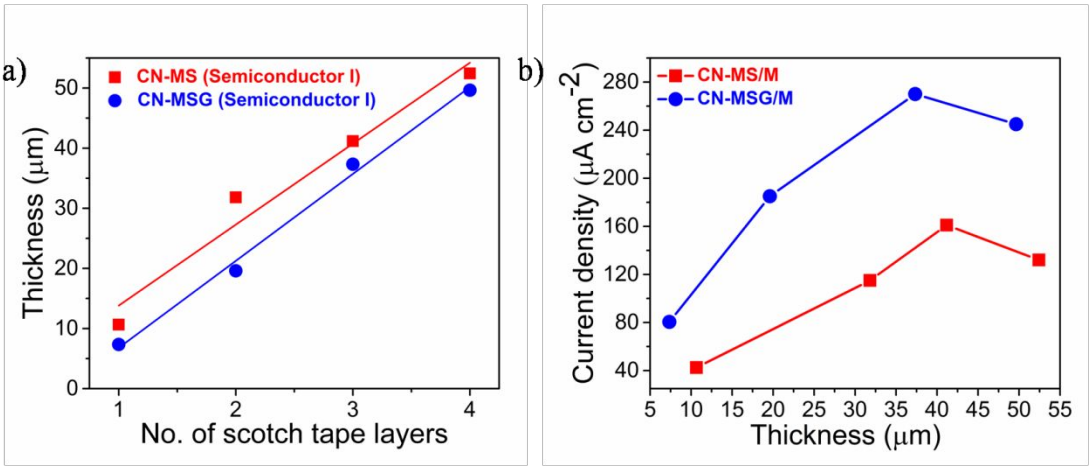

Figure S29. a) Relationship between the thickness and the scotch tape layer used for depositing first layers of CN (Semiconductor I). b) Photocurrent densities of CN-MS/M electrodes and CN-MSG/M of variable thickness in 0.1 M KOH (at 1.23 V *vs.* RHE) prepared by using 1–4 scotch tape layers.

The large diffusion length indicates that e^- can travel up to 40 μm without recombining with photogenerated h^+, which allows the use of a thick CN layer on the photoanodes. Further increase in the film's thickness (~50 μm) leads to lower photocurrent owing to the reduced light penetration and increased e^-–h^+ recombination before their collection (Figure S29).

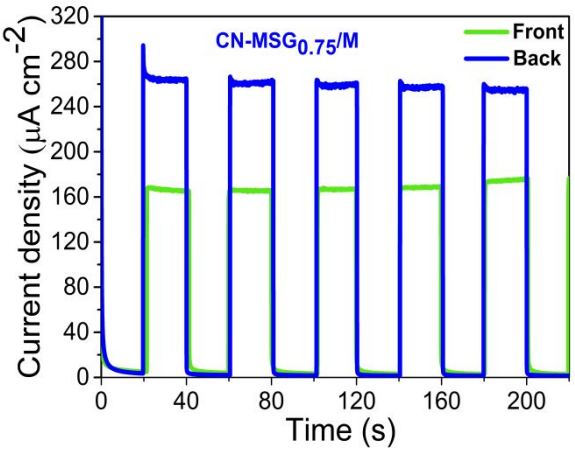

Figure S30. Photocurrent densities when illuminating from the front- and the back-side of CN-$MSG_{0.75}$/M (or CN-MSG/M) electrodes at 1.23 V *vs.* RHE electrode in 0.1 M KOH.

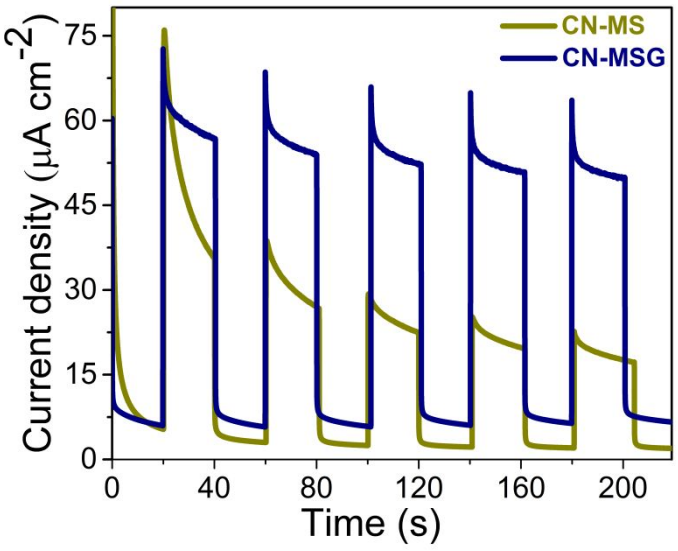

Figure S31. Photocurrent densities of CN-MS and CN-MSG photoanodes, which were prepared without melamine powder inside the tube.

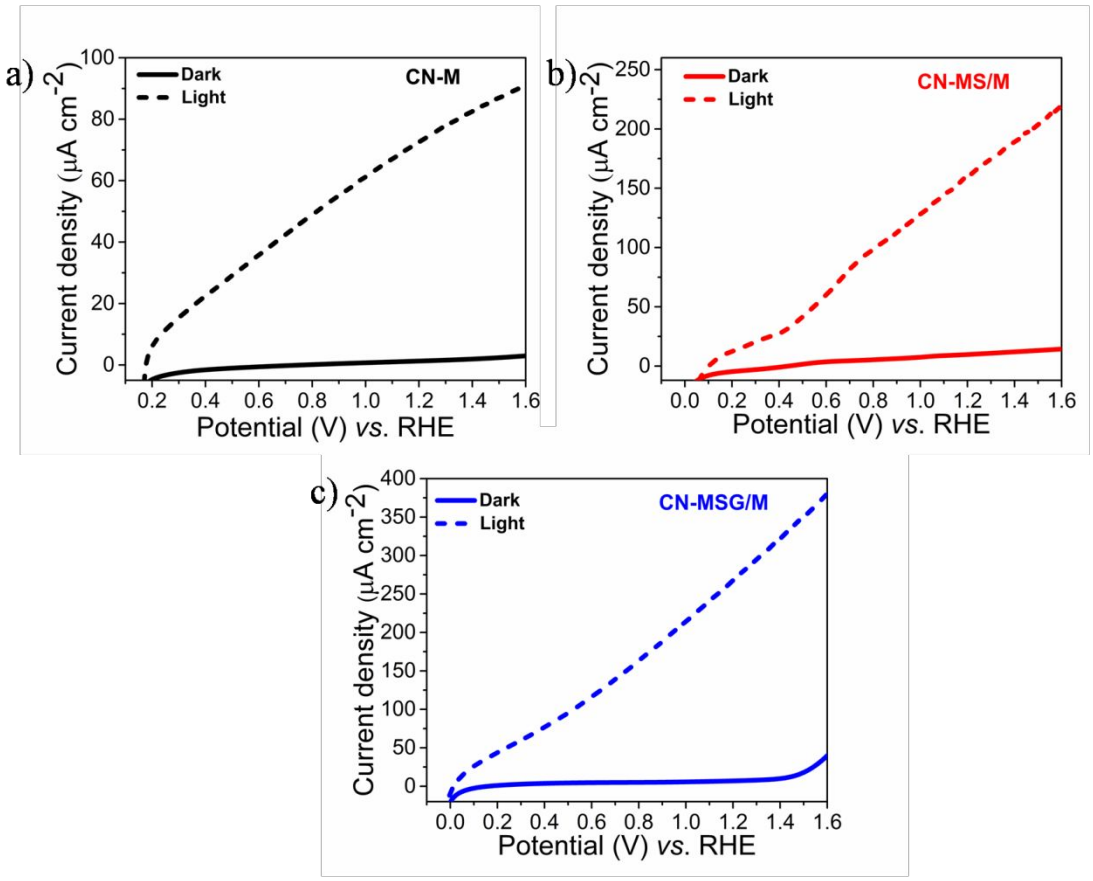

Figure S32. Linear sweep voltammetry (LSV) curves of CN (photo) anodes. a) CN-M, b) CN-MS/M, and c) CN-MSG/M in 0.1 M KOH (at 1.23 V *vs.* RHE) in the dark (solid lines) and under illumination (dashed lines).

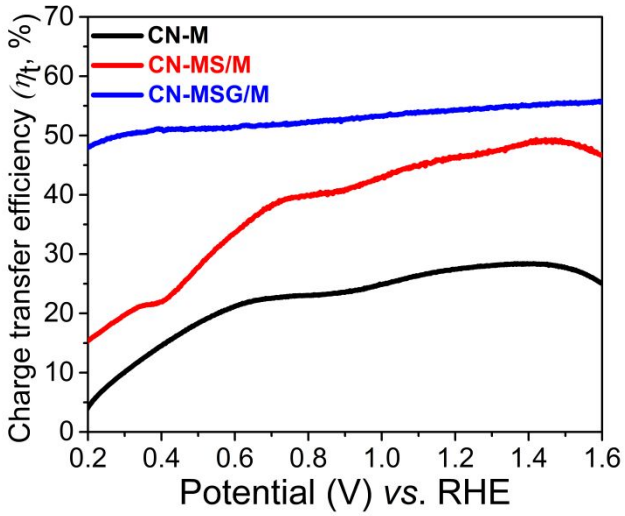

Figure S33. Charge transfer efficiency of CN electrodes, calculated by dividing the photocurrent obtained in 0.1 M KOH by the photocurrent obtained in 10% (v/v) TEOA containing 0.1 M KOH.

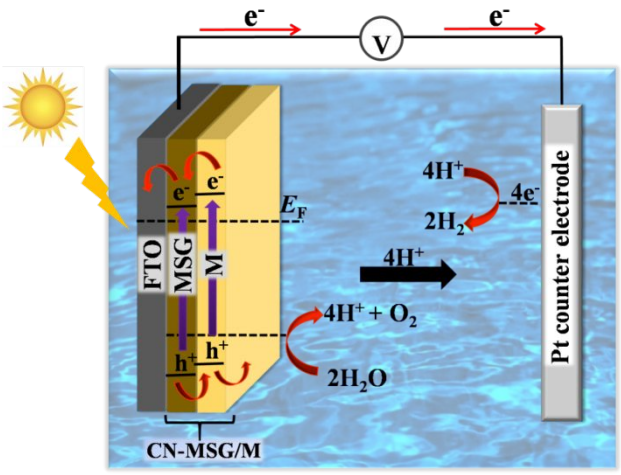

Figure S34. Possible mechanistic scheme for photoelectrochemical (PEC) water splitting.

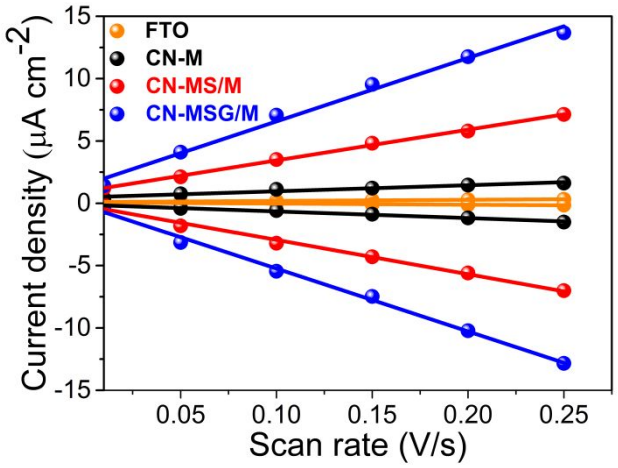

Figure S35. Cathodic and anodic charging currents of CN-M, CN-MS/M, and CN-MSG/M electrodes at 0.15 V *vs*. Ag/AgCl as a function of scan rate.

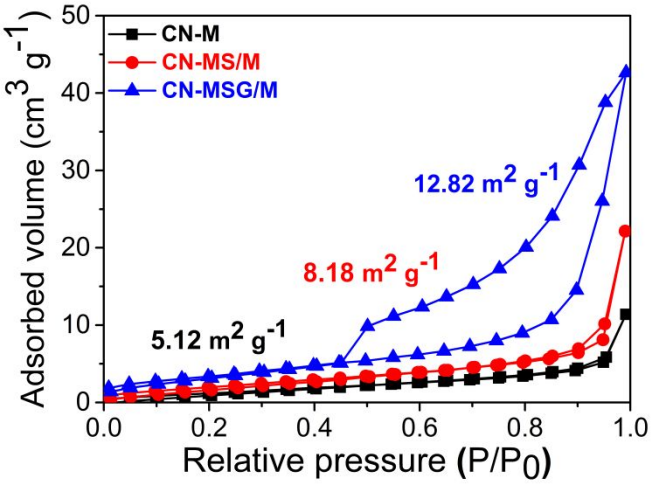

Figure S36. N_2 adsorption-desorption isotherms for CN electrodes (the actual experiments were performed by analyzing the relevant CN powder scratched from

FTO). The numbers (5.12, 8.18, and 12.82 m^2 g^{-1}) represent the specific surface area (of CN-M, CN-MS/M, and CN-MSG/M, respectively), which was calculated using the BET model.

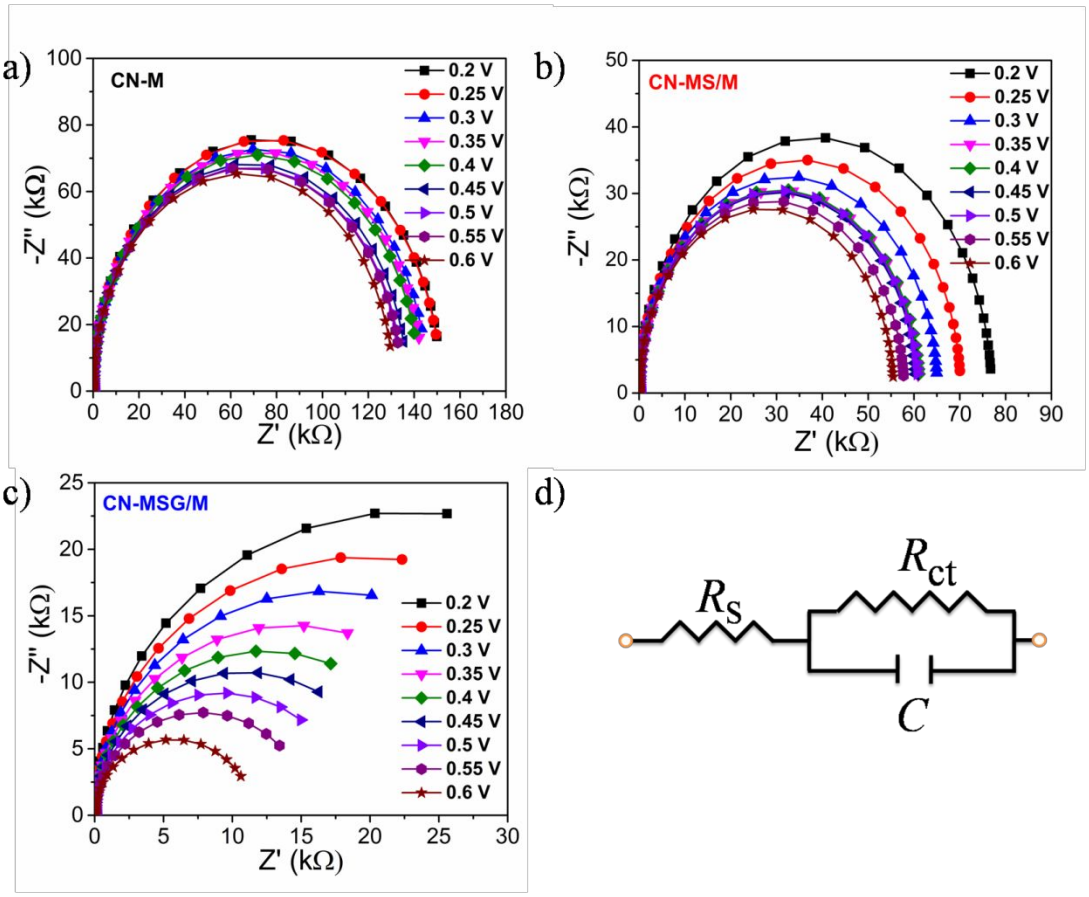

Figure S37. Nyquist plots at different potentials (*vs*. Ag/AgCl) in 0.1 M KOH aqueous solution of a) CN-M, b) CN-MS/M, and c) CN-MSG/M. (d) the equivalent circuit that was used for fitting: the R_{ct} values were obtained by fitting the semicircles of the Nyquist plots using this equivalent circuit.

Specifically, the R_{ct} of CN-MSG/M at 1.23 V *vs*. RHE is 4 times smaller than that of CN-M, which is attributed to the good charge-separation, owing to the conductivity of rGO, and better h^+ extraction properties, thanks to the close packing of the CN layers (Figure S37 and 5b).

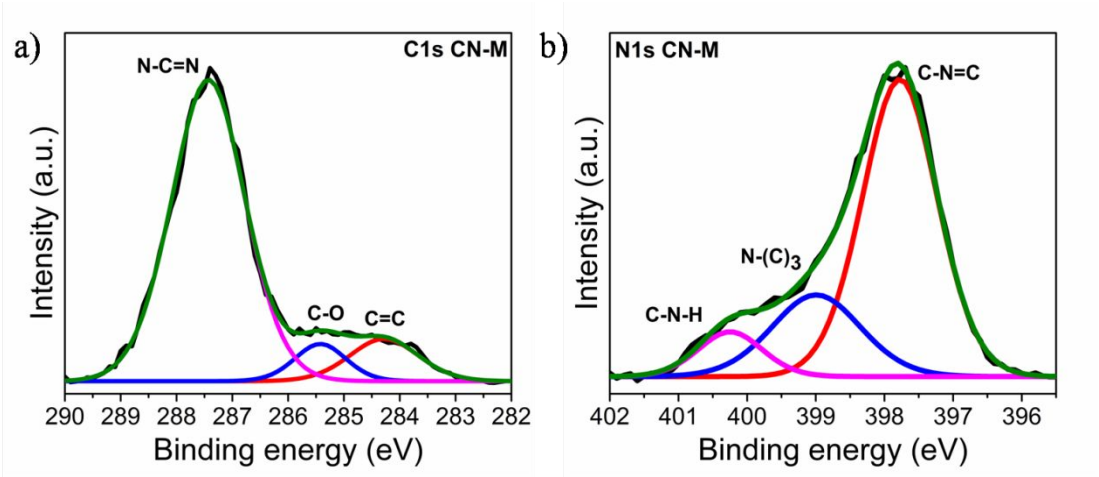

Figure S38. CN-M high-resolution XPS spectra after a stability test. a) C1s and b) N1s.

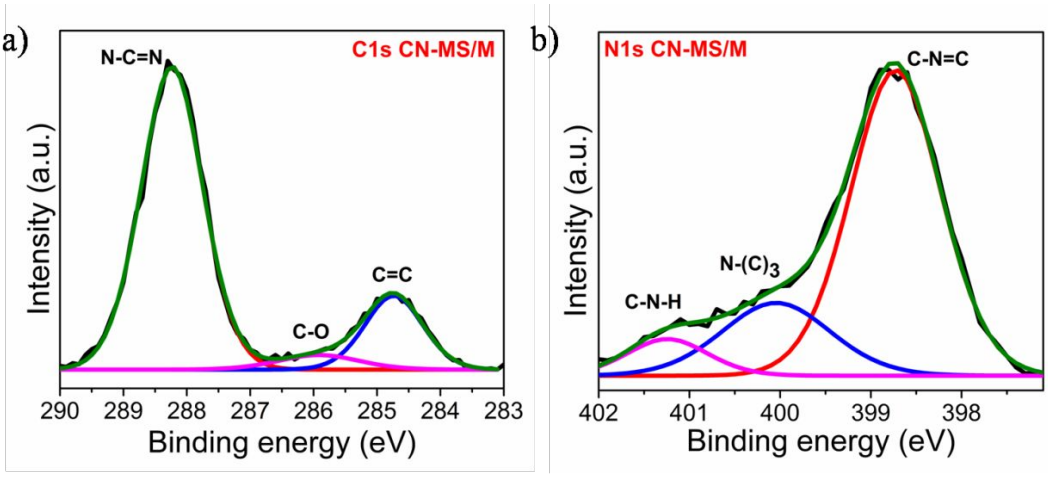

Figure S39. CN-MS/M high-resolution XPS spectra after a stability test. a) C1s and b) N1s.

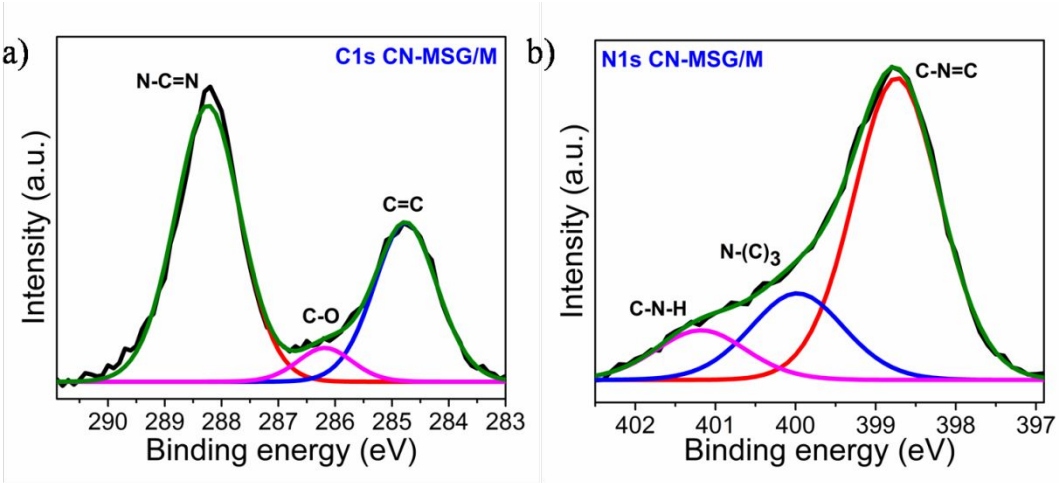

Figure S40. CN-MSG/M high-resolution XPS spectra after a stability test. a) C1s and b) N1s.

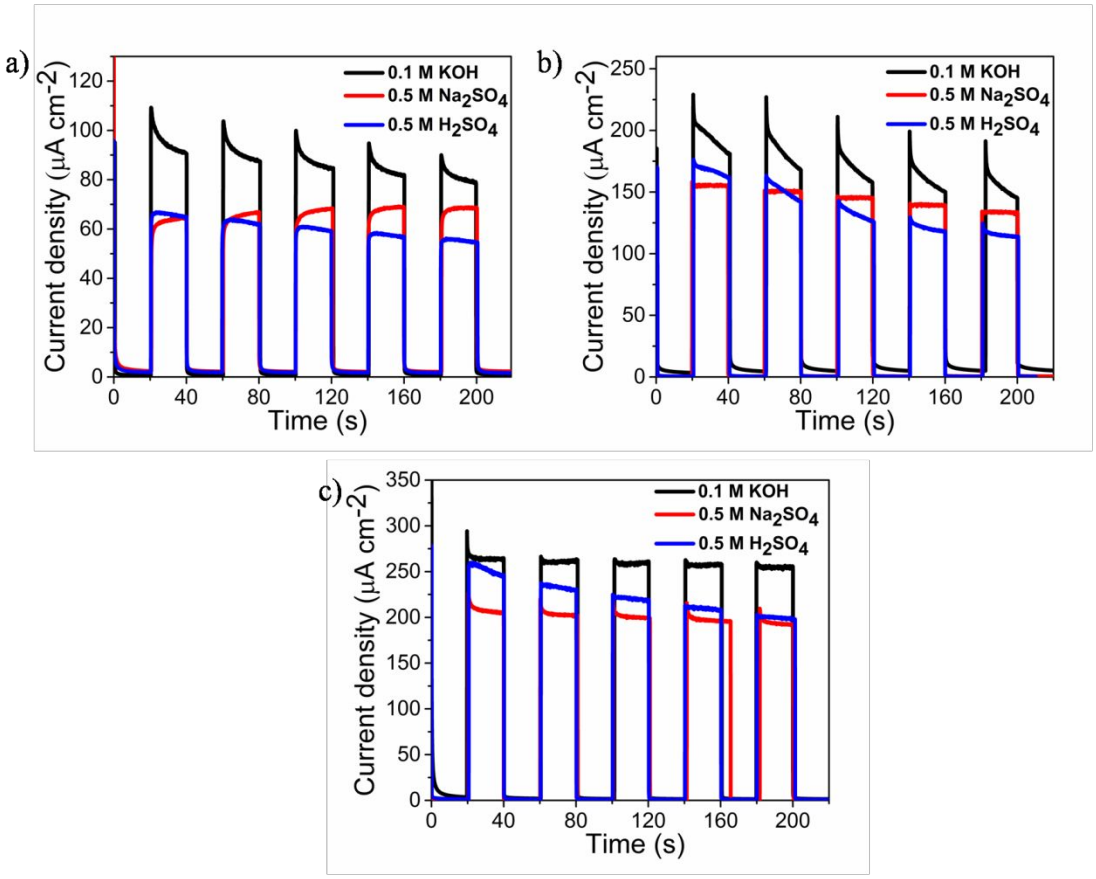

Figure S41. Photocurrent density of a) CN-M, b) CN-MS/M, and c) CN-MSG/M electrodes in different electrolytes, alkaline (0.1 M KOH, pH 13.1), neutral (0.5 M Na_2SO_4, pH 6.27), and acidic (0.5 M H_2SO_4, pH 0.27), represented by black, red, and blue, respectively).

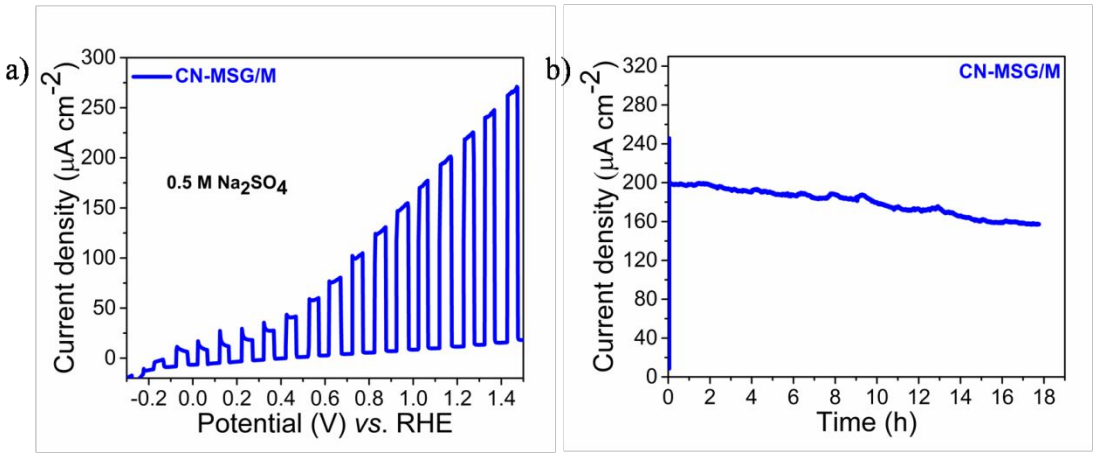

Figure S42. a) LSV curves of CN-MSG/M in 0.5 M Na_2SO_4 upon on/off illumination cycles. b) Photocurrent density of CN-MSG/M in 0.5 M Na_2SO_4 during 18 h.

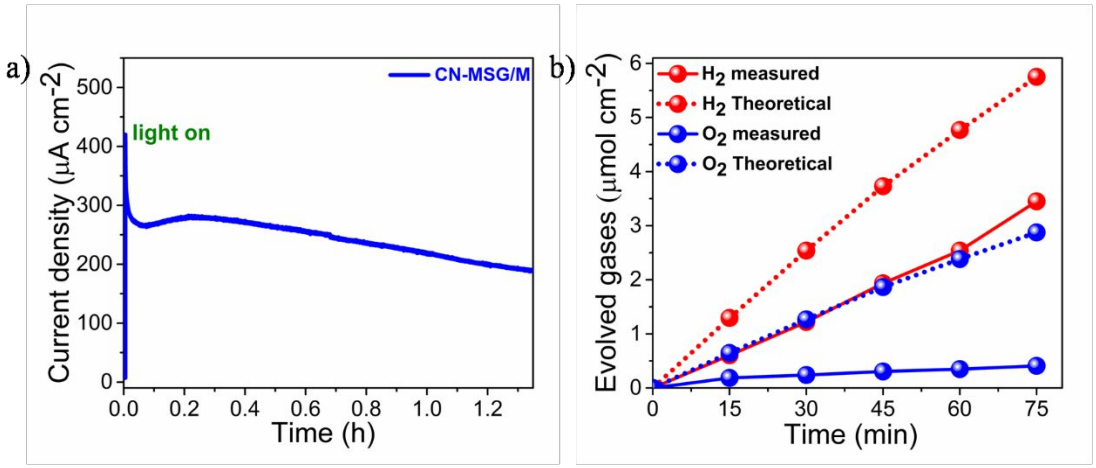

Figure S43. a) Photocurrent densities of CN-MSG/M electrodes (at 1.23 V *vs.* RHE) in 0.1 M KOH under 1-sun illumination for H_2 and O_2 evolution measurements. b) Evolution of H_2 and O_2 gases measured by gas chromatography (dashed lines correspond to the amount of H_2 ($e^-/2$) and O_2 ($e^-/4$) calculated from the photocurrent measurements). The Faradaic efficiency was obtained by comparing the amount of produced H_2 and O_2 with that of calculated H_2 and O_2.

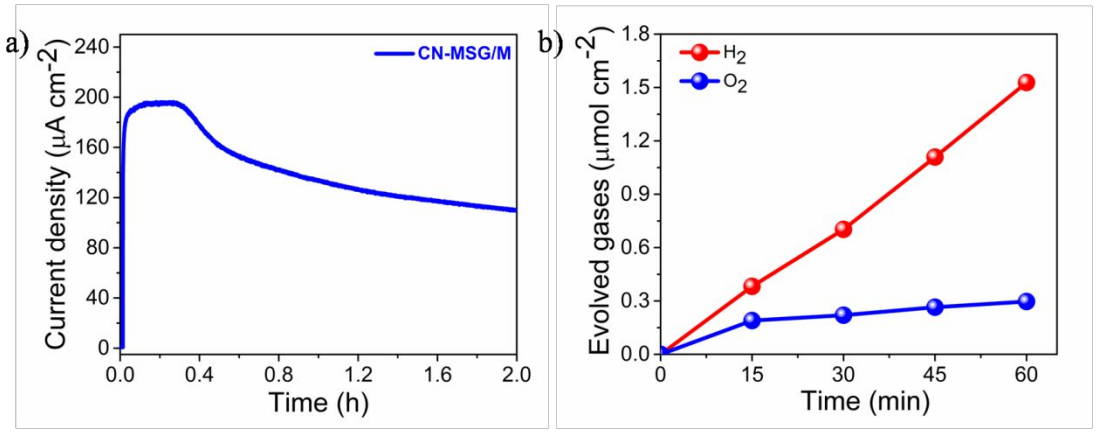

Figure S44. a) Photocurrent densities of CN-MSG/M electrodes (at 1.23 V *vs.* RHE) recorded in a phosphate buffer (0.1 M; pH 7) solution under 1-sun illumination for H_2 and O_2 evolution measurements. b) Evolution of H_2 and O_2 gases measured by gas chromatography (The calculated Faradaic efficiency of CN-MSG/M photoanode for H_2 and O_2 evolution was 50% and 19.4%, respectively).

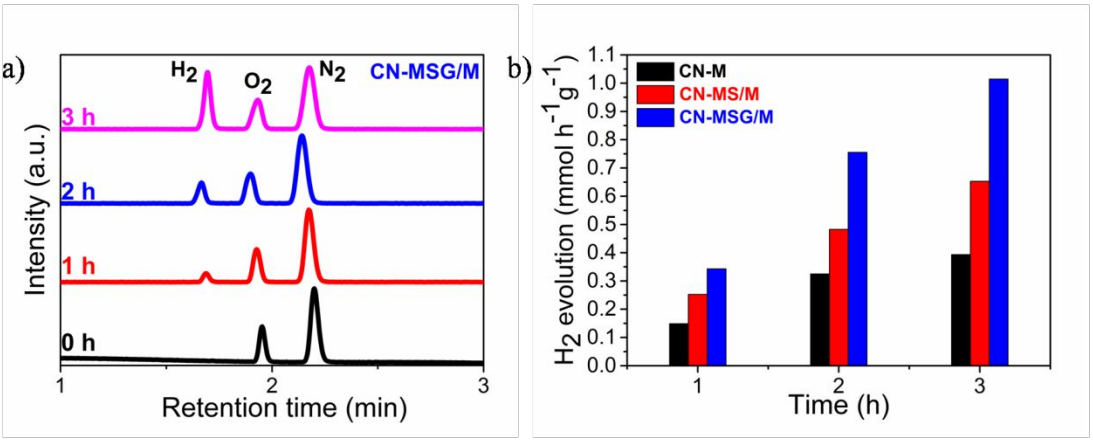

Figure S45. a) Gas chromatograph corresponding to the head space of the photoelectrochemical cell after different times of photocurrent density measurement with CN-MSG/M. The measurements were performed at 1.23 V *vs.* RHE, with 0.1 M KOH containing 10% (v/v) TEOA as an electrolyte. b) Specific H_2 production rates of CN electrodes as a function of time.

Table S2. PEC performance summary of CN-based photoanodes

CN photoanodes	Photocurrent at 1.23 V *vs.* RHE ($\mu A\ cm^{-2}$)	Onset potential *vs.* RHE	Electrolyte	Light intensity	Ref
CN-MSG/M	270	0.0012	0.1 M KOH	100 mW cm^{-2}, 1.5 AM	This work
	510	N/A	10% (v/v) TEOA in 0.1 M KOH		
CN-MS/M	160	0.06	0.1 M KOH	100 mW cm^{-2}, 1.5 AM	This work
	350	N/A	10% (v/v) TEOA in 0.1 M KOH		
In situ grown porous CN/rGO film	124.5	0.3	0.1 M KOH	100 mW cm^{-2}, 1.5 AM	[3]
	272	N/A	10% (v/v) TEOA in 0.1 M KOH		
Crystalline CN film	116	0.25	0.1 M KOH	100 mW cm^{-2}, 1.5 AM	[4]
	245	N/A	10% (v/v) TEOA in 0.1 M KOH	100 mW cm^{-2}, 1.5 AM	
P doped CN	120	N/A	1.0 M NaOH	100 mW cm^{-2}, 1.5 AM	[5]
CMD5 g-CN	100	N/A	0.1 M Na_2SO_4 + 0.1 M Na_2SO_3 + 0.01	100 mW cm^{-2}, 1.5 AM	[6]

			M Na_2S		
B-doped CN	102.3	~0.4	0.1 M Na_2SO_4	100 mW cm^{-2}, AM 1.5	[7]
S-doped CN	60	N/A	0.1 M KOH	50 W white light	[8]
CN–rGO film	72	0.75	0.1 M KOH	100 mW cm^{-2}, 1.5 AM	[9]
	660	N/A	10% (v/v) TEOA in 0.1 M KOH		
Crystal face g-CN	228.2	N/A	0.2 M Na_2SO_4	100 mW cm^{-2}, 1.5 AM	[10]
CN and P- and B-doped CN heterojunction	150	N/A	0.1 M Na_2SO_4	100 mW cm^{-2}, 1.5 AM	[11]
g-CN	63	N/A	0.1 M Na_2SO_4	100 mW cm^{-2}, 1.5 AM	[12]

Supporting Information References

[1] Karjule, N.; Barrio, J.; Tashakory, A.; Shalom, M. Bismuthiol-Mediated Synthesis of Ordered Carbon Nitride Nanosheets with Enhanced Photocatalytic Performance. *Sol. RRL* **2020**, 2000017.

[2] Dong, Y.; Pang, H.; Yang, H. B.; Guo, C.; Shao, J.; Chi, Y.; Li, C. M.; Yu, T. Carbon-Based Dots Co-doped with Nitrogen and Sulfur for High Quantum Yield and Excitation-Independent Emission. *Angew. Chem. Int. Ed.* **2013**, *52*, 7800-7804.

[3] Peng, G.; Qin, J.; Volokh, M.; Liu, C.; Shalom, M. Graphene Oxide in Carbon Nitride: From Easily Processed Precursors to a Composite Material with Enhanced Photoelectrochemical Activity and Long-Term Stability. *J. Mater. Chem. A* **2019**, *7*, 11718-11723.

[4] Peng, G.; Albero, J.; Garcia, H.; Shalom, M. A Water-Splitting Carbon Nitride Photoelectrochemical Cell with Efficient Charge Separation and Remarkably Low Onset Potential. *Angew.Chem. Int. Ed.* **2018***, 57,* 15807–1581.

[5] Fang, Y.; Li, X.; Wang, X. Phosphorylation of Polymeric Carbon Nitride Photoanodes with Increased Surface Valence Electrons for Solar Water Splitting. *ChemSusChem* **2019**, *12*, 2605-2608.

[6] Bian, J.; Xi, L.; Huang, C.; Lange, K. M.; Zhang, R. Q.; Shalom, M. Efficiency Enhancement of Carbon Nitride Photoelectrochemical Cells via Tailored Monomers Design. *Adv. Energy Mater.* **2016**, *6*, 1600263.

[7] Ruan, Q.; Luo, W.; Xie, J.; Wang, Y.; Liu, X.; Bai, Z.; Carmalt, C. J.; Tang, J. A Nanojunction Polymer Photoelectrode for Efficient Charge Transport and Separation. *Angew. Chem. Int. Ed.* **2017**, *56*, 8221-8225

[8] Xu, J.; Cao, S.; Brenner, T.; Yang, X.; Yu, J.; Antonietti, M.; Shalom, M. Supramolecular Chemistry in Molten Sulfur: Preorganization Effects Leading to Marked Enhancement of Carbon Nitride Photoelectrochemistry. *Adv. Funct. Mater.* **2015**, *25*, 6265-6271.

[9] Peng, G.; Volokh, M.; Tzadikov, J.; Sun, J.; Shalom, M. Carbon Nitride/Reduced Graphene Oxide Film with Enhanced Electron Diffusion Length: An Efficient Photo-Electrochemical Cell for Hydrogen Generation. *Adv. Energy Mater.* **2018**, *8*, 1800566.

[10] Xiong, W.; Chen, S.; Huang, M.; Wang, Z.; Lu, Z.; Zhang, R. Q. Crystal-Face Tailored Graphitic Carbon Nitride Films for High-Performance Photoelectrochemical Cells. *ChemSusChem* **2018**, *11*, 2497-2501.

[11] Luan, P.; Meng, Q.; Wu, J.; Li, Q.; Zhang, X.; Zhang, Y.; O'Dell, L. A.; Raga, S. R.; Pringle, J.; Griffith, J. C.; Sun, C.; Bach, U.; Zhang, J. Unique Layer-Doping-Induced Regulation of Charge Behavior in Metal-Free Carbon Nitride Photoanodes for Enhanced Performance. *ChemSusChem* **2020**, *13*, 328-333.

[12] Lv, X.; Cao, M.; Shi, W.; Wang, M.; Shen, Y. A New Strategy of Preparing Uniform Graphitic Carbon Nitride Films for Photoelectrochemical Application. *Carbon* **2017**, *117*, 343-350.